CHAPTER 6 CFD simulations and experimental results – Ceramic foam and orifice plates

6.1 Introduction

With the experimental and CFD shock tubes introduced in chapter five, this chapter reports on the results from the CFD simulations and the experimental tests using the shock tube. The shock tube was primarily used as a tool to produce shock waves that would impinge upon the porous media – ceramic foam – that was also discussed in chapter five. In most underground mining explosions, the shock wave precedes a flame front. Thus the ability of the porous media to allow the passage of the shock with as minimum as possible a pressure drop is important. Indeed, with the performance of the ceramic foam being the main source of investigation, a detailed description along with its material properties were given in chapter five.

Initial experimental and CFD simulations of the shock tube were given in chapter five. In chapter six, a more detailed results of the ceramic foam and the thin plate orifice plates are reported and discussed.

In order to arrest the flame, the porous media must be able to withstand the force of a shock wave and as part of the contribution to the body of knowledge, experimental tests and CFD simulations were carried out on various types of ceramic foams (with different pore per inch [ppi] values). These results from these simulations and tests will show the nature of the pressure drop across the various ceramic foams for a Mach number of approximately 1.5. This being the maximum attainable Mach number for the safe operation of the shock tube used in these tests.

The flexibility of CFD was such that the simulations were conducted by describing the shock tube flow as a two-dimensional problem. The CFD simulations showed the nature of the flow in the region of the porous media as well as giving more flexibility to investigate how various configurations of the obstructions placed in the porous region of

the CFD shock tube affected the magnitude of the pressure attenuation. Such flexibility is not achievable from experimental tests alone.

6.2 CFD simulation strategy

The general nature of the CFD software available means that most types of flow can be solved. This is usually done by using the appropriate numerical solution technique as briefly discussed in chapter four. It might not be necessary to describe every detail of the geometry or the flow and in fact it is usual practice to reduce the complexity of the problem by suitable modification to the original problem. The simplification of the problem depends on the aspect of the flow of interest, be it the contact surface or the shock front as in the shock tube problem. This simplification may be in terms of grid size, cell concentration or the numerical solution technique used.

Though the validation results for the shock tube flow without any obstructions in the porous region were given in the chapter five, the assumptions adopted for solving the flow problem with obstructions in the porous region were as follows: -

- the shock tube flow is described as one-dimensional in nature. The CFD simulations were conducted as two-dimensional in Rampant,

- though the shock tube problem is an inviscid flow problem, the presence of an obstruction produces reattachment problems downstream of the porous region. These observations were borne out in work carried out by Dwomoh and Dixon-Hardy (under review). The turbulent k-ε equations were used.

- the CFD simulations were all modelled as axisymmetric flow problems. Thus the obstructions were represented as a series of circular rings within the porous region. (They appear to be square or rectangular in section.)

These assumptions formed the basis of the CFD simulations of the ceramic foams for which the results are given in this chapter.

6.3 *Experimental procedure*

All the laboratory experiments in this research project were carried out using the custom-built shock tube in the Department of Mechanical Engineering at Brunel University.

All the measuring equipment and pressure gauges were calibrated and checked against the sensitivity values supplied by their manufacturers.

In order to achieve a fairly consistent set of results, each experiment was repeated up to a maximum of six times in succession. Also, more tests were conducted on different days checking for a consistent set of results from each test specimen.

The shock tube was loaded by filling the driver section with compressed air fed from a compressor until the pressure gauge atop the section registered 120 psi or approximately 8.38 bar. This was the maximum pressure used in all the tests as this was the safe maximum loading that the shock tube material could withstand. The diaphragm was then punctured when there were no air leaks and the data logging equipment was ready to record. The average values were then used for subsequent data analysis.

Before placing an obstruction (either orifice plate or ceramic foam) in the shock tube, incident pressure tests were always conducted in the first instance. This was to determine the strength of the pressure behind the shock wave as well as the magnitude of the pressure drop across the ceramic foam.

These incident pressure tests were performed as the location of the pressure transducers fore (70 mm before) and aft of the test region were such that the peak incident pressure values could not be reached before the appropriate pressure transducers detected the reflected pressure from the porous region. Figure 5.23 and Figure 5.24 show the pressure transducer readings for the incident pressure tests from the experimental shock tube, and the CFD shock tube. Figure 5.10 shows the pressure transducers in situ for an experimental incident pressure test.

All the experiments were conducted to determine the following pressures: -

- incident,

- reflected, and
- transmitted.

These pressure values would show the performance characteristics of the various ceramic foam and the orifice plates that were tested.

6.4 Orifice plate results

6.4.1 General

Initial CFD simulations with the single hole plates revealed that the sensor reading the transmitted pressure values in its current position - which was 70 mm downstream of the test section of the shock tube - would be reading lower than expected pressures. Such lower readings were due to the recirculation of the flow just downstream of the orifice plates. However, tests with the CFD model revealed that placing a sensor further downstream where the flow was fully developed, would eliminate the low reading problem. This was particularly useful as the tests were primarily concerned with the total pressure drop across the test specimen and not the pressure history of the flow field within the test section. The sensor on the experimental shock tube was moved to a new location, 210 mm downstream of the test section. Thus all transmitted pressure values are taken from a sensor placed at this location.

The experimental and CFD results for the orifice plates are discussed based on several assumptions, namely: -

- the incident pressure value is constant throughout the experimental tests. This is shown in the plots by normalising the pressure values where applicable.
- the diaphragm pressure ratio was consistently 8.38:1 for the experimental tests,

Based on these assumptions the following points can now be discussed in detail. These assumptions do not apply to the ceramic foam experiments.

6.4.2 Consistency of experimental results

For each configuration, a maximum of six tests were carried out and the average values taken. However, these tests were then repeated at different times when the temperature and atmospheric pressure might have changed slightly. This was done to check the degree of repeatability of the results taken by the pressure transducers in their respective locations. Figure 6.1 shows the incident pressure tests carried for during the tests with all three sensors located on the same radius but at 90° angles from each other. These tests were always carried out before testing with the ceramic foams or an orifice plate was in situ.

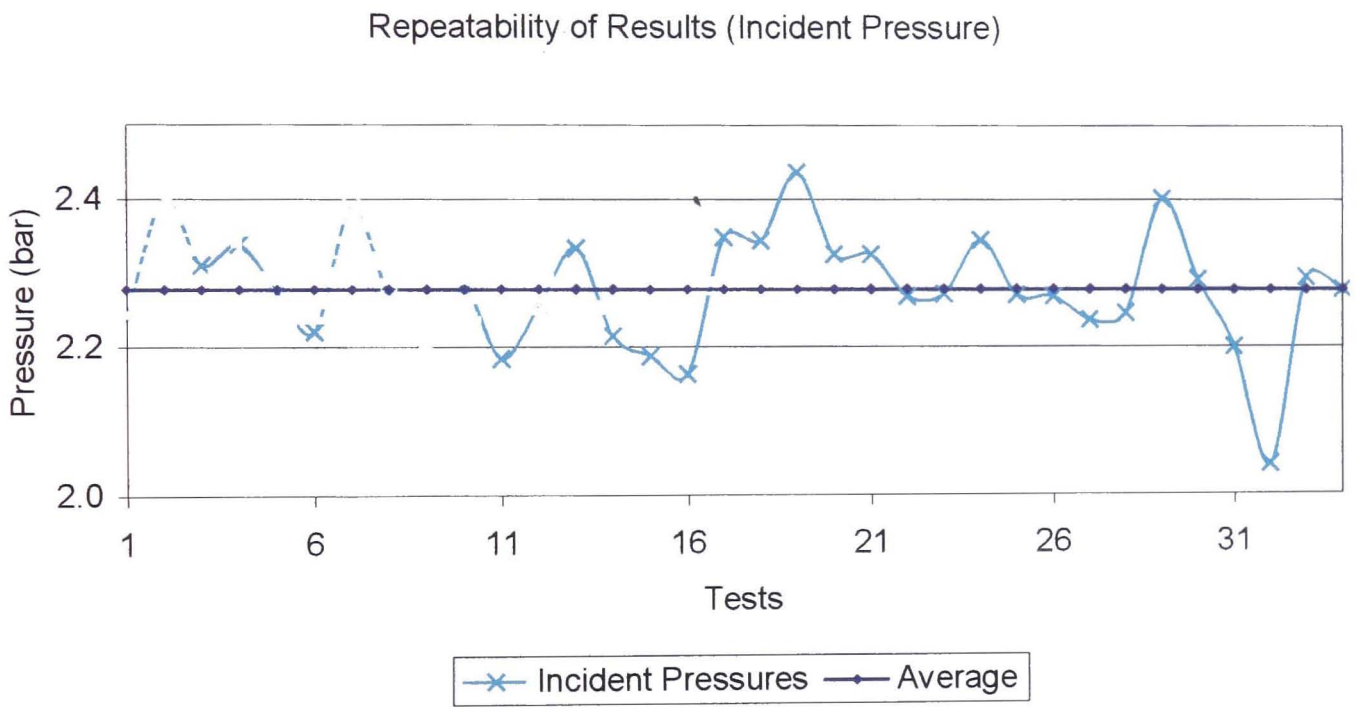

Figure 6.1 – Repeatability of experimental results.

Figure 6.1 shows the average pressure readings for the various tests performed on the orifice plates and the ceramic foam. The incident pressure values were taken before each test and also on different days. The average incident pressure was approximately 2.3 bar with a maximum of 2.438 bar and a minimum incident pressure magnitude of 2.042 bar.

However, in all tests, the incident pressure used was that obtained in the incident pressure tests conducted prior to testing on the test specimen.

6.4.3 Experimental orifice plate results

One of main areas of this research was to determine the pressure drop across various ceramic foam and correlate this with that across various orifice plates. The aim of such an exercise would be a significant contribution to the body of knowledge. This is borne out by the fact that the ceramic foam is used in the castings industry where the pressure drop is not of interest. In fact most research in the castings industry seems to concentrate on flow rates and the pore sizes as shown by Sutton et al[92].

However, in the design of the explosion door such comparison data would be a useful aid to determine the characteristics of the ceramic foam when a shock wave impinges upon it.

Using the internal diameter of the experimental shock tube as 55 mm, all the blockage areas (BA) for the orifice plates were calculated based on the total area of the 2 mm thick plate. The nominal area of the 55 mm diameter plate is 2375.83 mm^2. As an example, to calculate an 80% BA orifice plate would entail determining the required single hole diameter, which in this instance is 24 mm. Thus the 80% BA orifice plate would have a single 24 mm diameter hole. (See Figure 5.22).

However, various multiple hole configurations of orifice plates with the same blockage area were also tested and the holes sizes for these were all calculated by calculating the diameter of each hole based on the total area for an 80% BA. These multiple hole configuration tests were conducted to check the influence of such a configuration on the pressure drop across an orifice.

Table 6.1 shows the configurations of the orifice plates tested.

The blockage areas are such that as the BA value gets closer to zero more of the orifice plate is open thereby allowing more of the flow to pass through. Also the areas are such that as the BA value decreases, the number of different hole configurations per orifice plate BA also decreases as shown by the 40% and 30% BAs.

Table 6.1 Orifice plate configurations.

Blockage Area, % ↓	Configuration (number of holes) and hole diameters (mm)			
	1	2	4	9
30	45	/	/	/
40	42	/	/	/
50	38	/	14	/
60	34	/	17	11
70	30	/	15	10
80	24	17	12	8

The tests were conducted with the transmitted pressure sensor moved to a location that was 210 mm from the porous region/orifice plate. The reasons for such a move have been discussed earlier in section 6.4.1.

All the results shown are average tests for six consecutive tests. Where there were two pressure transducers (as in the incident and reflected pressure values) an average value was used.

6.4.4 CFD simulations of the orifice plates

The advantages from a CFD simulation are the ability to change parameters such as boundary conditions, pressures, temperatures, and density. Also the real life problem can be simplified (where the geometry is complex) by certain assumptions such as a two-dimensional representation of the problem. Finally, the graphical results obtained from a CFD simulation give an insight into the behaviour of the fluid in the domain of interest, where experimental results only give the behaviour of the fluid at a series of points where pressure transducers are located.

As such, the CFD simulations were also to give an insight into the nature of the flow through the orifice plates and the ceramic foam as well as checking against the experimental results.

The nature of shock tube flow is that it is always modelled as a one-dimensional problem. This is due to the flow being heavily dominated by convection in the x-direction. However, the Rampant CFD code can model problems as either two-dimensional, three-dimensional or axisymmetric. Thus all the CFD tests were solved as axisymmetric flow problems. This allowed the investigation of the changes in the fluid properties (pressure, temperature, and density) along the radial and axial directions of the shock tube.

Assuming axisymmetric flow meant that only single orifice plates could be investigated and not the multiple orifice variety for the purposes of symmetry.

In the CFD simulations, two 'sensor' points were positioned on the wall of the shock tube to represent the location of the sensors on the experimental shock tube. The data from these points were saved at every iteration and analysed using Microsoft Excel. One iteration is one time step, Δt. The time step is related to the Courant number and the mesh size. As the peak values of the data is of most interest, the real time for the simulations were not used in plotting the results especially as one could not define this time step easily. However, information regarding the time can be obtained at every iteration. The data files from the CFD simulation results were also analysed such that the behaviour of the shock could be readily viewed especially as it passed through the orifice.

6.4.5 CFD grid sensitivity tests

Prior to the CFD simulations, grid sensitivity tests were conducted. The purpose of such tests is to determine what mesh size will eventually lead to a grid-independent solution. Grid sensitivity tests are conducted by changing the node distribution along the edges of the geometry. Thus a fine mesh will have a much denser node distribution than a coarse mesh. As it is essential to capture the nature of the problem in detail and ensure accurate results, the grid must strike a balance between being too fine and too coarse. Especially

as too fine a mesh can cause numerical errors and too coarse a mesh will also fail to accurately represent the shock tube flow.

In grid sensitivity tests, there are several parameters of fluid flow that could be used to determine the effectiveness of the final grid. In a problem dealing with gas dynamics, the accurate representation of the contact surface is important as there is a temperature change across it. In this research, as pressure is the parameter of importance, its accurate resolution is paramount. Thus in these tests, the main criteria was the incident pressure value as this could be determined analytically as shown in chapter 4.

In the grid sensitivity tests, the shock wave was resolved over a few grid cells when the correct incident pressure was obtained.

The results revealed that the chosen mesh for the orifice plates test gave an incident pressure value, which was within 1% of the analytically derived value for an 8.38:1 diaphragm pressure ratio. Though a finer mesh would have reduced the incident pressure to the analytical value as well as resolve the shock wave within a few cells, the gains would be outweighed by the computational effort required to solve the problem. The same mesh size was used in all subsequent tests for the orifice plates.

6.4.6 Pressure attenuation results – orifice plates

The following results are the average values for a series of simulations conducted on each specimen. The CFD results were for one test only as there is no need to check for a repeatable set of results – not until the boundary conditions changed or the geometry is modified. In this case, neither of the two scenarios was encountered as the grid and conditions were common to all tests. As the contribution to the body of knowledge is an insight into the performance characteristics of the ceramic foam with the explosion door, all the results give an indication of the incident pressure, the reflected pressure, and the transmitted pressure magnitudes.

The experimental incident pressure values are taken from the average of the three sensors that are mounted on the same circumference, but at 90° angles from each other.

Analytically the incident pressure for a diaphragm pressure of 8.37:1 is approximately 2.65 bar. However, the difference between this value and the CFD results are such that the same CFD grid was used throughout the orifice plate tests.

6.4.6.1 30% BA experimental and CFD results

The experimental 30% BA tests were conducted on a single hole orifice plate, as there were no other configurations that would give the required blockage area.

Table 6.2 – Results for a 30% BA orifice plate.

Configuration	Incident Pressure, bar	Reflected Pressure, bar	Transmitted Pressure, bar
CFD	2.662	4.862	2.358
1 hole	2.355	3.964	2.094

6.4.6.2 40% BA experimental and CFD results

The experimental 40% BA tests were conducted on a single hole orifice plate, as there were no other configurations that would give the required blockage area.

Table 6.3 – Results for a 40% BA orifice plate.

Configuration	Incident Pressure, bar	Reflected Pressure, bar	Transmitted Pressure, bar
CFD	2.660	5.312	2.276
1 hole	2.278	4.540	2.036

6.4.6.3 50% BA experimental and CFD results

With a 50% BA, the hole sizes were such that two configurations – a single hole, and a four hole orifice plate were tested.

Table 6.4 - Results for a 50% BA orifice plate.

Configuration	Incident Pressure, bar	Reflected Pressure, bar	Transmitted Pressure, bar
CFD	2.663	5.832	2.217
1 hole	2.278	5.170	1.964
4 holes	2.205	5.163	2.029

6.4.6.4 60% BA experimental and CFD results

Three configurations representing a 60% BA were tested – a single hole, four hole, and a nine hole orifice plate. The tests were conducted on different days thus the different incident pressure values.

Table 6.5 - Results for a 60% BA orifice plate.

Configuration	Incident Pressure, bar	Reflected Pressure, bar	Transmitted Pressure, bar
CFD	2.661	6.281	2.030
1 hole	2.278	5.793	1.756
4 holes	2.205	5.722	1.745
9 holes	2.205	5.665	1.762

6.4.6.5 70% BA experimental and CFD results

As with the 60% BA test, the same types of orifice plate configuration were tested for the 70% BA orifice plate tests.

Table 6.6 - Results for a 70% BA orifice plate.

Configuration	Incident Pressure, bar	Reflected Pressure, bar	Transmitted Pressure, bar
CFD	2.661	6.714	1.884
1 hole	2.265	6.553	1.582
4 holes	2.205	6.585	1.474
9 holes	2.259	6.423	1.593

6.4.6.6 80% BA experimental and CFD results

Four configurations of the 80% BA orifice plate were tested. This was made possible by the fact that the diameters of the holes were small enough. Thus a single hole, a twin hole, a four hole, and a nine hole configuration were all tested.

Table 6.7 - Results for a 80% BA orifice plate.

Configuration	Incident Pressure, bar	Reflected Pressure, bar	Transmitted Pressure, bar
CFD	2.659	7.197	1.645
1 hole	2.265	7.487	1.314
2 holes	2.328	7.347	1.293
4 holes	2.259	7.377	1.301
9 holes	2.328	7.327	1.336

6.5 Discussion of experimental results and CFD simulations – Orifice plates

Figure 6.2 shows a reading from an experimental result using a 50% BA four hole orifice plate. The data acquisition software filters the original and electronically noisy signals and the pressure values used in the analysis are from the filtered signals. The two higher

values signals are from the pressure transducers reading the incident/reflected pressures. These transducers were positioned 70 mm upstream of the test section of the shock tube and on the same radial axis. The third signal from the transmitted pressure sensor was located 210 mm from the test section of the shock tube.

6.5.1 Increasing the blockage area (BA)

The effect of a higher value BA as discussed section 6.4.3 simulates a more restricted orifice for the shock wave to pass through. As such, the reflected pressure is expected to increase and the transmitted pressure to decrease as the BA value increases. This can be seen in Figure 6.3. The pressure values are normalised to take into account the slight variation in the incident pressures used during the tests.

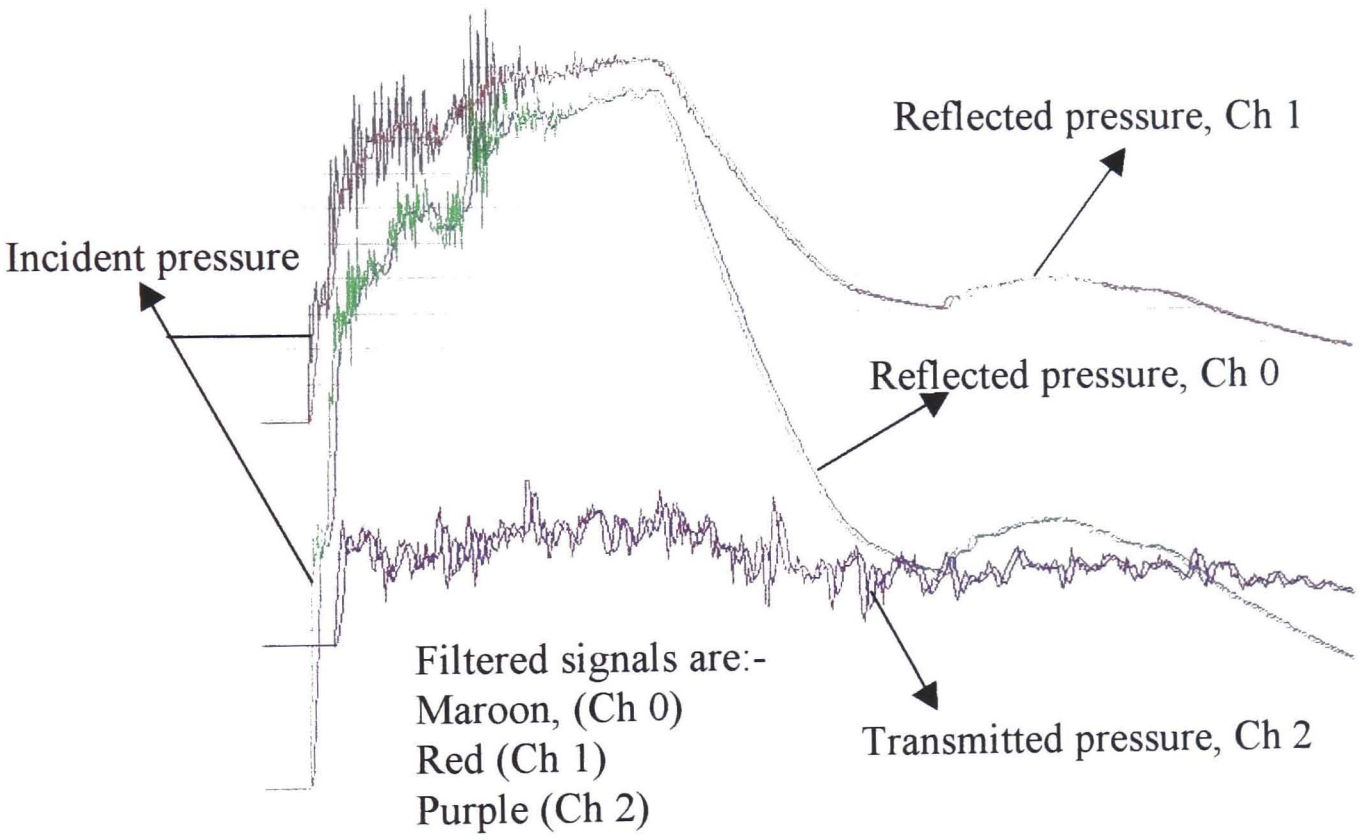

Figure 6.2 – Typical orifice plate reading from the Data acquisition system – LabView.

The results show that not only does the reflected pressure increase as the BA value increases but there is a fairly good agreement between the experimental and CFD simulations. However, as the blockage area increases there is a deviation between the CFD simulations and experimental results for the reflected pressures. It was noted in the

experimental results that increasing the BA value for the orifice plates caused severe oscillations and that this could be the reason for the discrepancy between the CFD simulations and experimental reflected values. Also the reflected pressure sensors were located 70 mm from the orifice plates and that could be subjected to severe vibrations as the shock tube dissipated the energy in the shock wave when the BA values were large. Note that the transmitted pressure sensor was placed 210 mm downstream of the test section of the experimental shock tube.

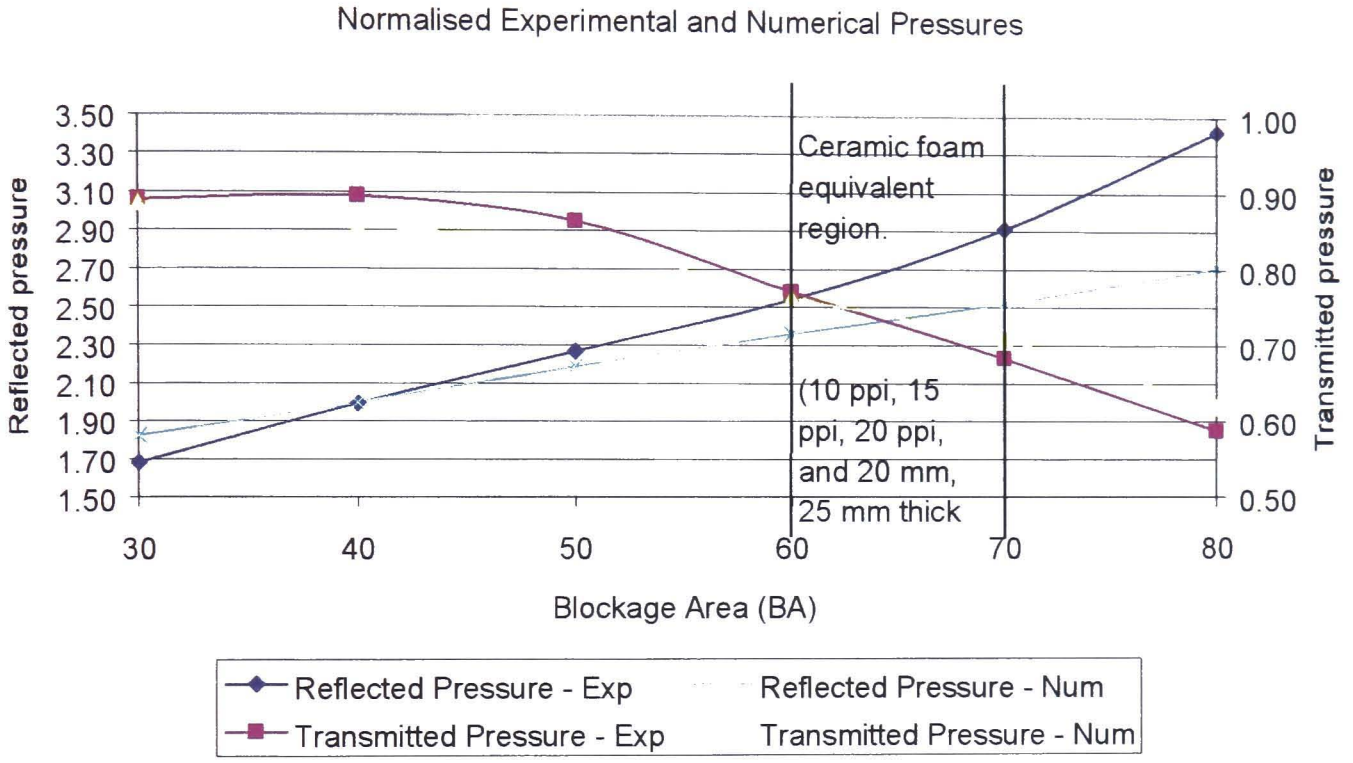

Figure 6.3 – Normalised CFD and experimental pressures for single orifice plates.

In Figure 6.3, the normalised values are calculated by dividing the reflected and transmitted pressure values by the incident pressure values. These data used in this figure are for the single hole configuration orifice plates.

In order to mitigate the effects of the higher incident pressure values from the CFD simulations, the results from the CFD simulation and the experimental tests are normalised.

Analysing the normalised results show that there is a close agreement between the CFD simulations and the experimental tests for the transmitted pressure values for the various blockage area orifice plates. However, the reflected pressure values are not is such close

agreement. In the experimental tests, the reflected pressures have rather high values and these induce severe oscillations (discussed in section 6.5.3) within the shock tube. Thus there is more energy to be dissipated to the shock tube walls, which distort the true reflected pressure values.

In this research, the transmitted pressure is of most interest. The pressure drop across the ceramic foam, and the orifice plates will give a useful insight into the ability of the ceramic foam to attenuate shock waves. The discrepancies in the reflected pressure results are not deemed that important.

6.5.2 Multiple hole configurations – orifice plates

The ceramic foam is made up of a series of icosahedral structures across its surface area. A regular icosahedron has twenty equal faces, with each face representing an equilateral triangle. (See Figure 6.4). As such, it can be thought of as representing a multiple hole configuration orifice plate. Testing multiple hole configurations of each single hole orifice plate was deemed necessary to investigate the performance of the thin orifice plates compared with the ceramic foam, and the behaviour of the shock wave in the vicinity of the various configurations. Also, the multiple hole orifice plates were tested to determine to determine the effect of the hole configuration on the pressure attenuation characteristics of each plate.

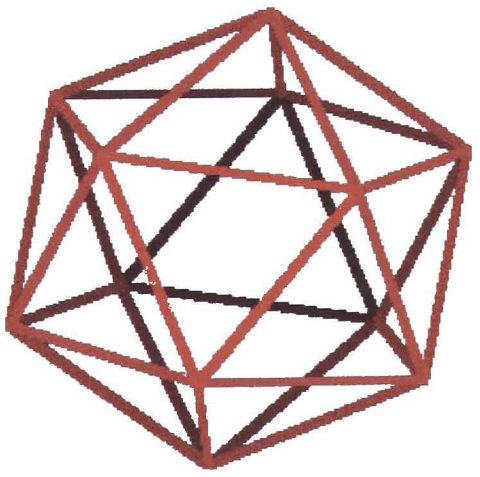

Figure 6.4 – An icosahedral structure.

Figure 6.5 shows the bar chart comparison between the multiple and single hole configurations. The higher values represent the reflected pressure values and the lower values are for the transmitted pressure through the orifice plates. As stated earlier, the configurations were single hole, twin hole, four hole, and nine hole orifice plates depending on the BA value of the orifice plate. Normalised pressure values less than 1.5 refer to the transmitted pressure for the various orifice plates. Those normalised values greater than 1.5 refer to the reflected pressures. Figure 6.5 shows that there is minimal difference between the configuration and the performance of an orifice plate.

Table 6.8 shows one standard deviation for the results as well as the normalised mean values for the experimental results. This shows that there is a consistency in the reproduction of the orifice plate test results. The low standard deviation values also show that given the same blockage area, the differences are rather small to make any significant impact on their interpretation. Thus it is assumed that the pressure change as the shock wave impinges upon the various plates is not dependent on the hole configuration of the orifice plate. This could be borne out by the fact that the area of the orifice plate open to allow for the passage of the shock wave is always similar in all configurations.

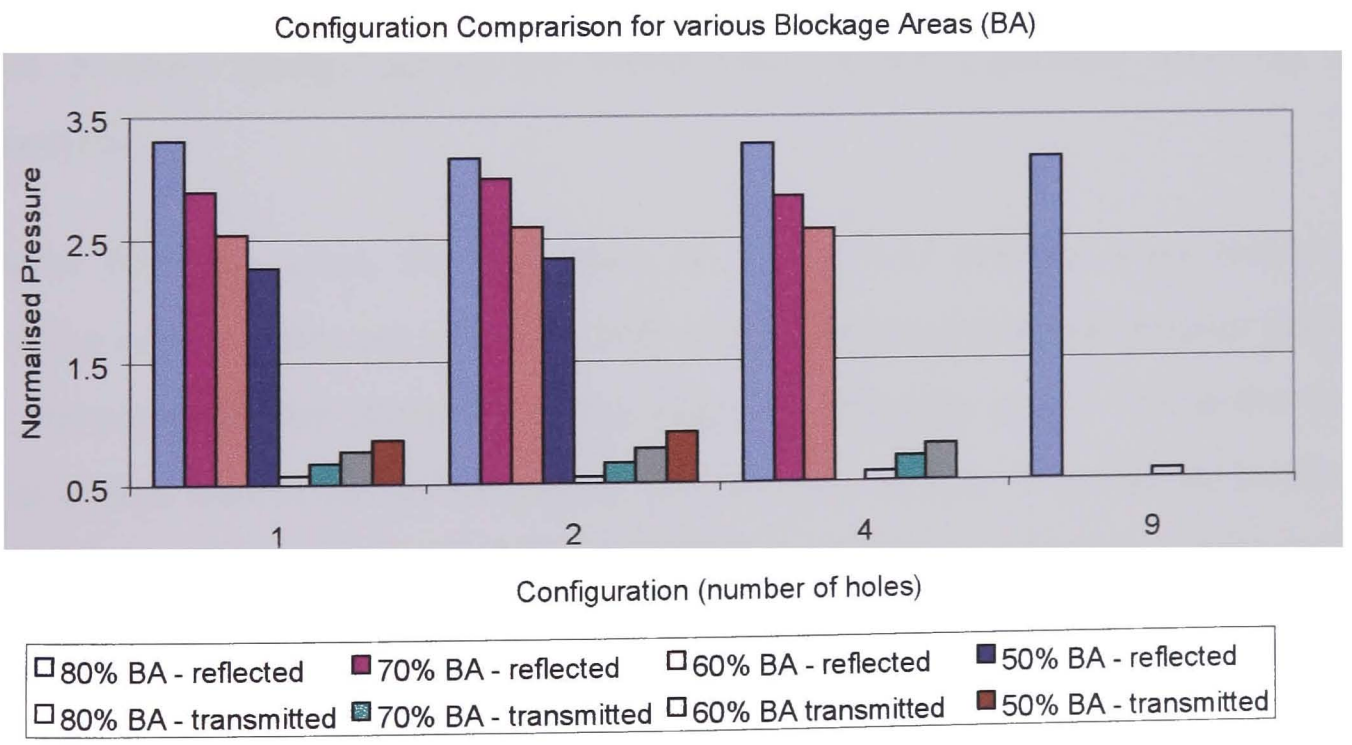

Figure 6.5 – Multiple/single hole configuration tests results.

As in Figure 6.3, the normalised values are obtained by dividing the incident and reflected pressure values by the respective incident pressure values.

Table 6.8 – Consistency of the orifice plate experimental results.

Configuration	Standard Deviation - Reflected/Transmitted	Mean -Reflected/Transmitted (Normalised)
50%	0.051/0.041	2.306/0.891
60%	0.026/0.015	2.569/0.787
70%	0.073/0.019	2.908/0.685
80%	0.079/0.011	3.219/0.571

For the lower value blockage areas, the number of configurations is two per orifice plate, increasing to three for the higher value configurations. The reason for this was explained earlier and is primarily due to space restrictions on the area of the orifice plate.

6.5.3 Pressure drop across the orifice plates

The following discussions on the pressure drop across the orifice plates are based on the results of the single hole orifice tests. As reiterated earlier, the experimental results show that the pressure change across the orifice plate is not dependent upon the hole configuration.

At smaller blockage areas, the proportion of the incident pressure wave transmitted through the orifice plates are relatively high when compared with the incident pressure values; the pressure drop across the orifice plates are relatively small. This is due to the fact that a large area of the orifice plate is still open to the flow with a rather small area representing an obstruction. Also the energy of the shock wave does not have a large obstruction over which to dissipate, thereby allowing the shock wave to pass through the thin orifice plate almost unhindered. This observation is borne out by Figure 6.6.

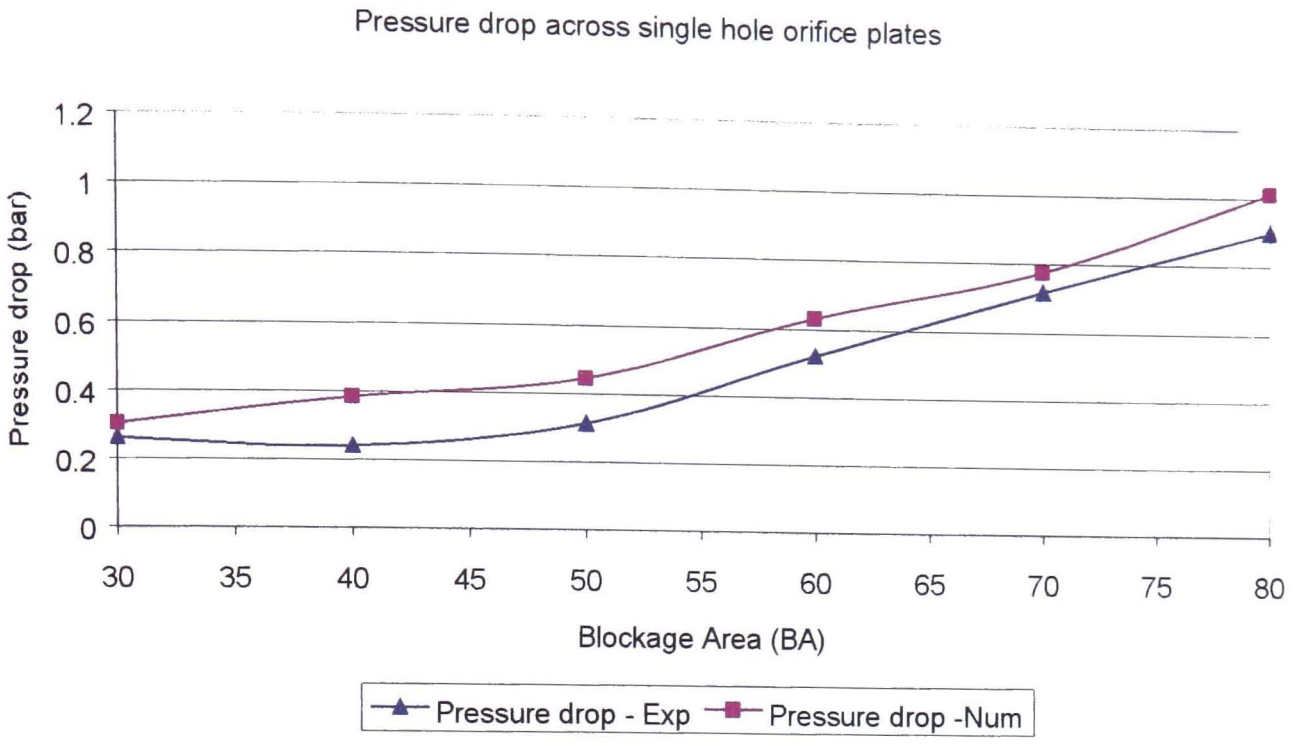

Figure 6.6 – Experimental and CFD pressure drop across the orifice plates.

Here the plot shows that as the orifice plate gets more restrictive – decreasing hole diameter and increasing BA value, the pressure drop increases as the transmitted pressure gradually decreases. However, this is to be expected as the more of the incident pressure is reflected and very little of it is transmitted. This behaviour would continue until the thin orifice plates had a BA value close to 100, representing a totally blocked shock tube. An experimental observation made during the tests was the severe oscillations that were caused by the shock wave impinging upon the orifice plates, especially pronounced as the blockage area increased. The severity of these oscillations was directly related to the blockage area of the orifice plates. (See Figure 6.7).

The CFD simulation results also exhibit a similar pattern of behaviour to that of the experimental results. The differences in the values could be due to the assumptions made earlier, and possibly experimental errors.

Figure 6.8 shows a CFD pressure contour plot of an orifice plate with a 50% blockage area. This plot shows a similar profile to the orifice plate simulations. The shock wave has impinged upon the orifice plate and the region upstream of the orifice plate shows the magnitude of the reflected pressure. The transmitted pressure region is just downstream of the orifice plate and the normal incident shock wave is distorted. The

presence of the orifice plates turns the normal shock wave into something akin to a bow wave in the area just downstream of the orifice plate. However, further downstream, the shock wave becomes a normal wave with a reduced pressure magnitude travelling behind it.

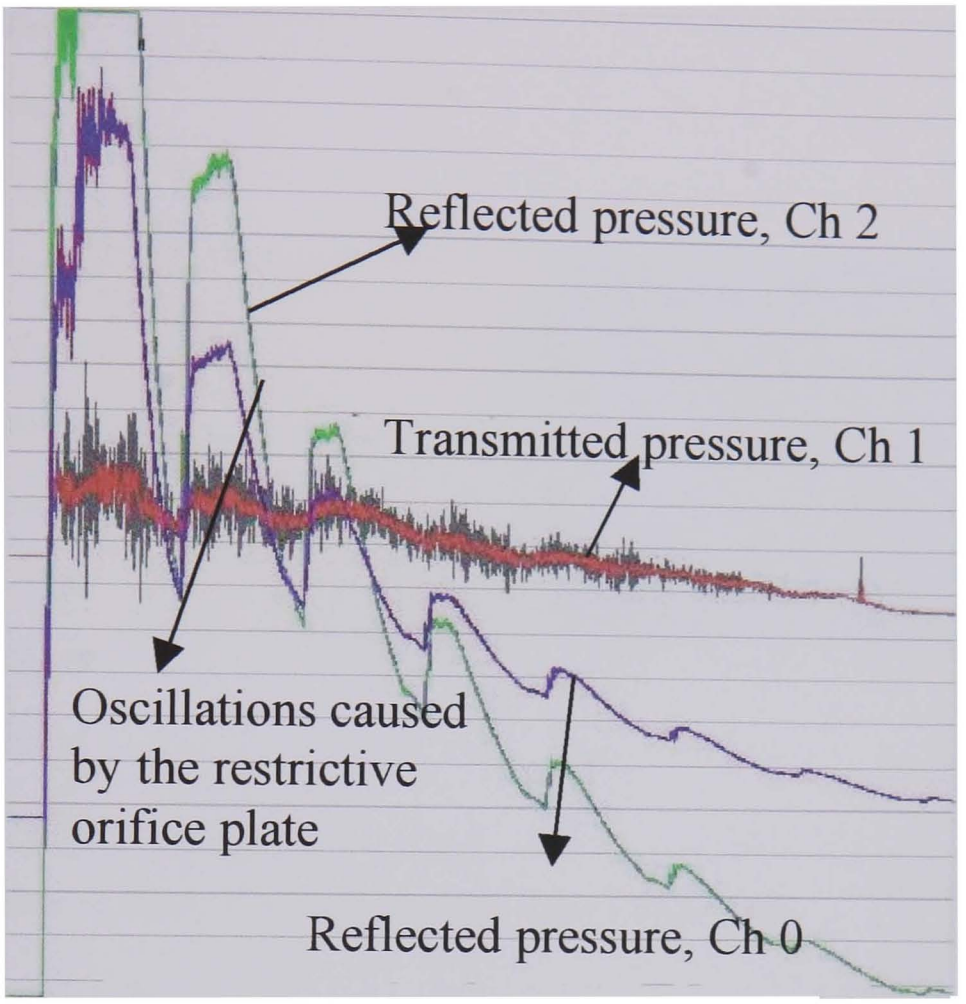

Figure 6.7 – Orifice plate signal showing severe oscillations.

Figure 6.9 shows the CFD simulation plot of a 60% BA orifice plate. This plot shows a similar profile to the orifice plate simulations. The CFD sensor records the arrival of the incident pressure wave and its magnitude almost instantaneously – there is a change in the pressure from atmospheric to the pressure behind the shock. Once the shock has impinged upon the orifice plate and has been reflected, the sensor (reading the incident and reflected pressure values) detects the arrival of the reflected shock wave with another increase in its pressure value. The sharp rise in pressure is followed by an asymptotic rise to a peak value. The transmitted pressure sensor detects the passage of the transmitted pressure with a sudden increase in pressure above atmospheric. Here the rise after the arrival of the shock, there is less of an asymptotic rise to a peak value. This

is due to the reduction in the strength of the transmitted shock wave. Though the CFD sensor plots give a very small section of the nature of the flow within the shock tube, there is a correlation between these plots and that from the experimental shock tube, see Figure 6.2.

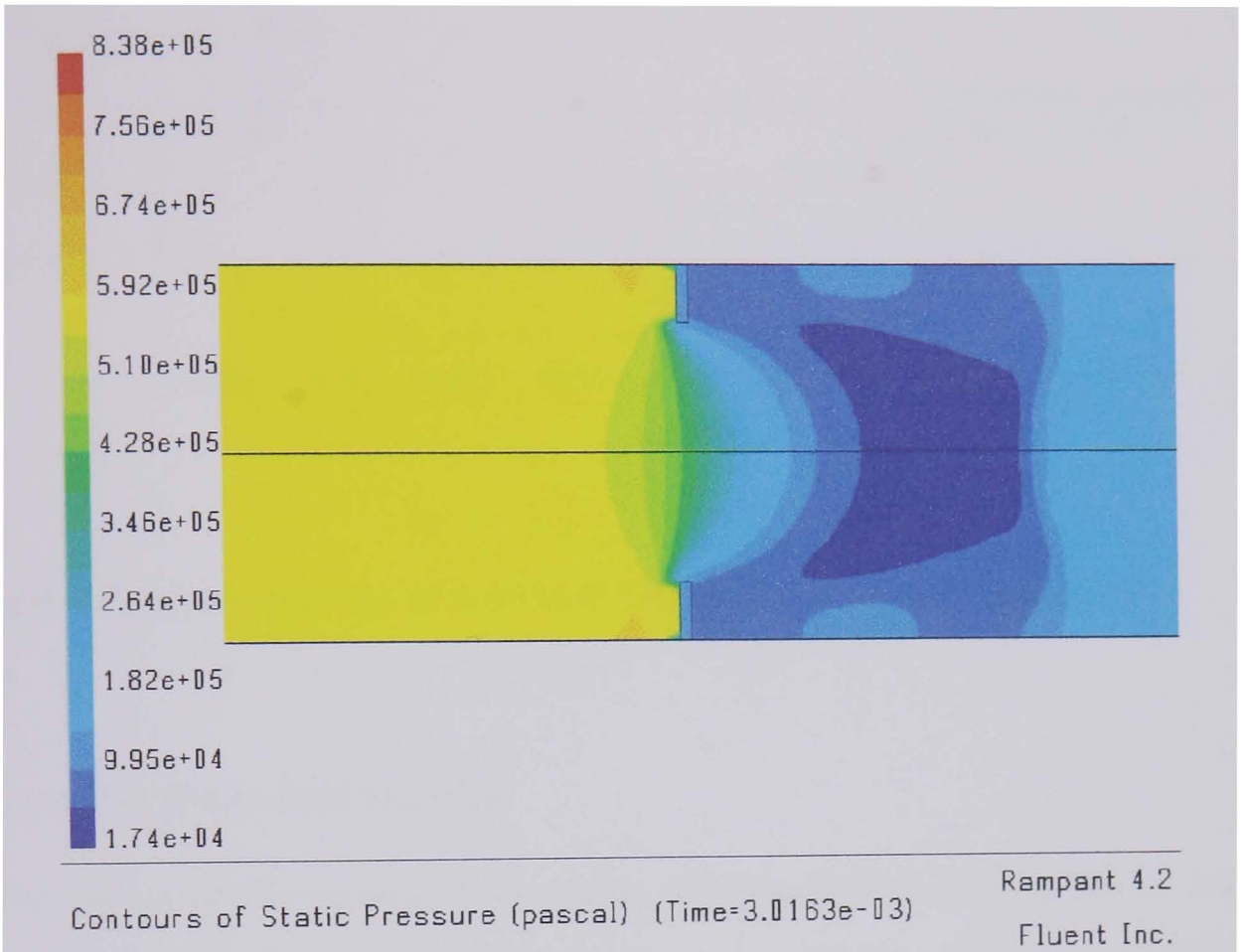

Figure 6.8 – Sample CFD orifice plate pressure contour plot – 50% BA.

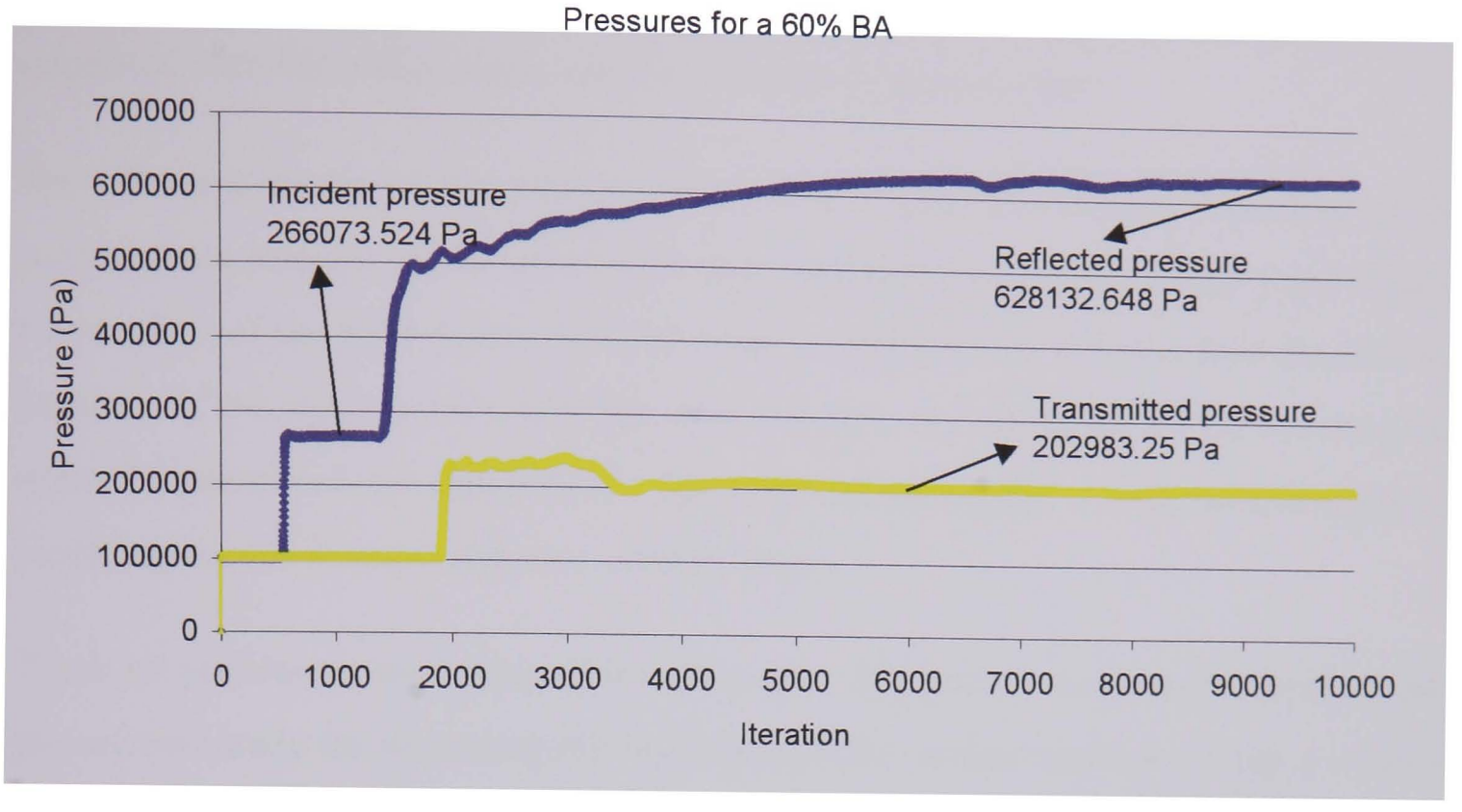

Figure 6.9 – Pressure history of a 60% BA orifice plate CFD simulation.

6.6 Ceramic foam test results

The performance of the ceramic foam under loading from a moving shock wave is of prime importance to this research. Such a loading will determine the suitability of the ceramic foam as a porous material for the explosion door and, what useful information can be obtained about its ability to attenuate shock waves. The incident shock wave in these experiments were around Mach 1.5. The ceramic foam used in these tests was manufactured from Zirconia (Zirconium Oxide – ZrO_2) and has been described in detail in section 5.4 of previous chapter five. In this section, characteristics such as the pressure drop, velocity attenuation, the effect of varying the thickness of the ceramic foam on pressure attenuation, pore size and its effect on pressure drop, as well as a CFD equivalent of the ceramic foam will be reported and discussed.

6.6.1 General

As with the thin orifice plate tests, the pressure transducers were located in the same position on the shock tube for consistency. This was not particularly necessary as the

CFD simulations of the ceramic foam revealed that the flow attachment problems associated with the orifice plates were not evident in this test case.

The following results are the average values for a series of simulations conducted of the ceramic foam samples. CFD simulations were performed using the sample 1 and sample 4 equivalent of the CFD foam. Sample 1 had a diameter that was less than the internal diameter of the shock tube whilst the other samples all had diameters greater than the internal diameter of the shock tube. Thus, modelling sample 4 was representative of modelling the other larger diameter ceramic foams.

There are reasons for modelling samples 1 and 4. The porous media model in Rampant, the software code for simulating the flow through the ceramic foam could not accurately describe the flow, thus a different approach to modelling the flow was devised as discussed in section 5.4.1. This approach relied on the number of points on each face of the ceramic foam, equivalent to the number of points representing the solid portions of the ceramic foam. The points increased as the ppi value increased making it more difficult to count the number of points on the face of the 15 ppi and 20 ppi ceramic foams. Thus in order to simulate the effects of changing the ppi value, the sample 1 ceramic foam was modelled with various air porosities. The decreasing air porosity value representing an increasing ppi value ceramic foam. See section 6.7.4 for a discussion on the effects of changing the air porosity of the CFD models of the sample 1 ceramic foam.

The air porosity of the CFD model for sample 1 was changed in order to determine its effect on the pressure reflected and transmitted pressure. Changing the air porosity value entailed a change in the size of the obstructions representing the ceramic foam in the ceramic foam simulations. Increasing the size of the obstructions was akin to a ceramic foam with a higher air porosity value.

In performing the CFD simulations and experimental tests on the various ceramic foam, several assumptions had to be made and the following discussions are based on these assumptions: -

- the diaphragm pressure ratio was consistently 8.38:1, thus the incident pressure value is constant in all the experimental tests,
- the CFD model is a fairly accurate representation of the experimental tests, and
- the strength of the shock means that there is no dissipation of the shock wave along the radius of the ceramic foam in the experimental tests.

These assumptions formed the basis for a discussion of the results from the ceramic foam CFD simulations and the experimental tests. These assumptions do not apply to the orifice plate experiments.

6.6.2 Experimental

Experimental data from the ceramic foam tests would not only help with the design of the explosion door, it would also serve to illustrate the advantages or otherwise of Zirconia as the porous material. Zirconia is currently used as a filtering medium in the castings industry where flow rates and pore size are the prime parameters of importance. In arresting explosions in an underground mining environment, the ability of the ceramic to attenuate the shock wave without being destroyed and thus subsequently stopping the flame front behind the shock wave is the principal requirement.

Thus, as in the orifice plate tests, samples of the ceramic foam were placed in special fixtures. These were designed such that they were held securely with only the internal area of the shock tube exposed and positioned in the shock tube such that it was impinged upon by an assumed planar shock wave once the diaphragm separating the driver from the driven section was punctured.

Several tests were conducted on each ceramic foam sample to check for reproducible and consistent results. Each sample was tested a maximum of six times during each test session, and the average reflected and transmitted pressure values recorded using the data acquisition software, LabView.

6.6.3 CFD simulations of the ceramic foam

The complex nature of the ceramic foam coupled with the fact that the porous media model in Rampant (the CFD software used for the CFD simulations) could not accurately represent the flow through the porous media meant that the porous media model was not used. The porous media model does not represent the physical volume obstructions created by the presence of the ceramic foam. The porous media model instead represents the ceramic foam by a momentum sink which means that the transient flow within the porous media is not possible. Such a representation could not be used as the object of the experimental tests and the CFD simulations was to investigate the pressure characteristics across the ceramic foam and the orifice plates. However, a suitably modified approach to modelling the ceramic foam had to be adopted. This approach took into account the thickness of the samples, the air porosity, and the number of points on each face. These were then used to create a series of obstructions that presented a physical reduction in volume within the shock tube. (See section 5.4.1 for a more detailed discussion on the CFD model of the ceramic foam).

6.6.4 Results – ceramic foam

The experimental incident pressure values are taken from the average of the three sensors that are mounted on the same circumferential axis but at 90° angles from each other. Analytically the incident pressure for a diaphragm pressure of 8.38:1 is approximately 2.65 bar. CFD simulations showed the incident pressure to have a magnitude of approximately 2.64 bar. The difference between the experimental value and that from the CFD simulation is very small. As such the same CFD grid was used throughout the porosity change simulations for the sample 1 ceramic foam. As with the experimental shock tube, 'sensors' were located 70 mm upstream and 210 mm downstream of the test section to record the incident and reflected pressure, and the transmitted pressure respectively. Data from these points were saved at every iteration during the solution simulation process and analysed using Microsoft's Excel software.

Table 6.9 shows the CFD simulation and experimental results for the various ceramic foams tested. Two CFD simulations of the ceramic foam were based on the dimensions of the sample 1 and sample 4 ceramic foam. The CFD model of the sample 4 ceramic foam would be similar in geometry to the ceramic foams bar sample 1, thus it was not necessary to model them. The CFD results are shown in brackets.

Table 6.9 - Results for ceramic foam – experimental and CFD simulations.

	Sample 1	Sample 2	Sample 3	Sample 4	Sample 5	Sample 6
Incident Pressure, bar (CFD)	2.350 (2.640)	2.259	2.259	2.309 (2.650)	2.309	2.309
Reflected Pressure, bar (CFD)	7.930 (5.678)	6.250	6.125	5.599 (6.435)	5.893	6.097
Transmitted Pressure, bar (CFD)	1.422 (1.894)	1.584	1.551	1.655 (1.925)	1.527	1.432

Table 6.10 – Properties of the ceramic foams used in the experimental tests.

	Diameter, mm	Thickness, mm	Porosity, ppi
Sample 1	50	20	10
Sample 2	75	25	15
Sample 3	100	20	20
Sample 4	125	25	10
Sample 5	125	25	15
Sample 6	125	25	20

Samples 1, 2, and 3 are all conical in section, whereas the remaining samples were conical in section with the smaller diameter being 100 mm and the larger diameter, 125 mm. As reiterated earlier, special fixtures were designed to secure the ceramic foams within the test section of the shock tube and ensure minimal loss in pressure. Table 6.10 shows the geometrical and some physical properties of the ceramic foam.

The assumption that the flow can be modelled as a one-dimensional problem is true as long as there are no changes in the radial direction of the flow domain. Figure 6.10 shows the velocity distribution in the radial axis of the shock tube. The variations in the velocity in the porous region show that the flow cannot be described as one-dimensional due to the presence of the obstructions. The blocks representing the obstructions are closer to the centre line surface from which the data for the plots are taken. This means that the flow has to traverse a very narrow region, hence the increase in velocity.

In fact as will be discussed later, (see Figure 6.14), it can be seen that the obstructions within the test section are very close to the fixture walls and the symmetry line. It is in this narrow gap that the flow velocity in the radial direction increases dramatically, making the problem two-dimensional. Downstream of the porous region, there is very little flow in the radial direction.

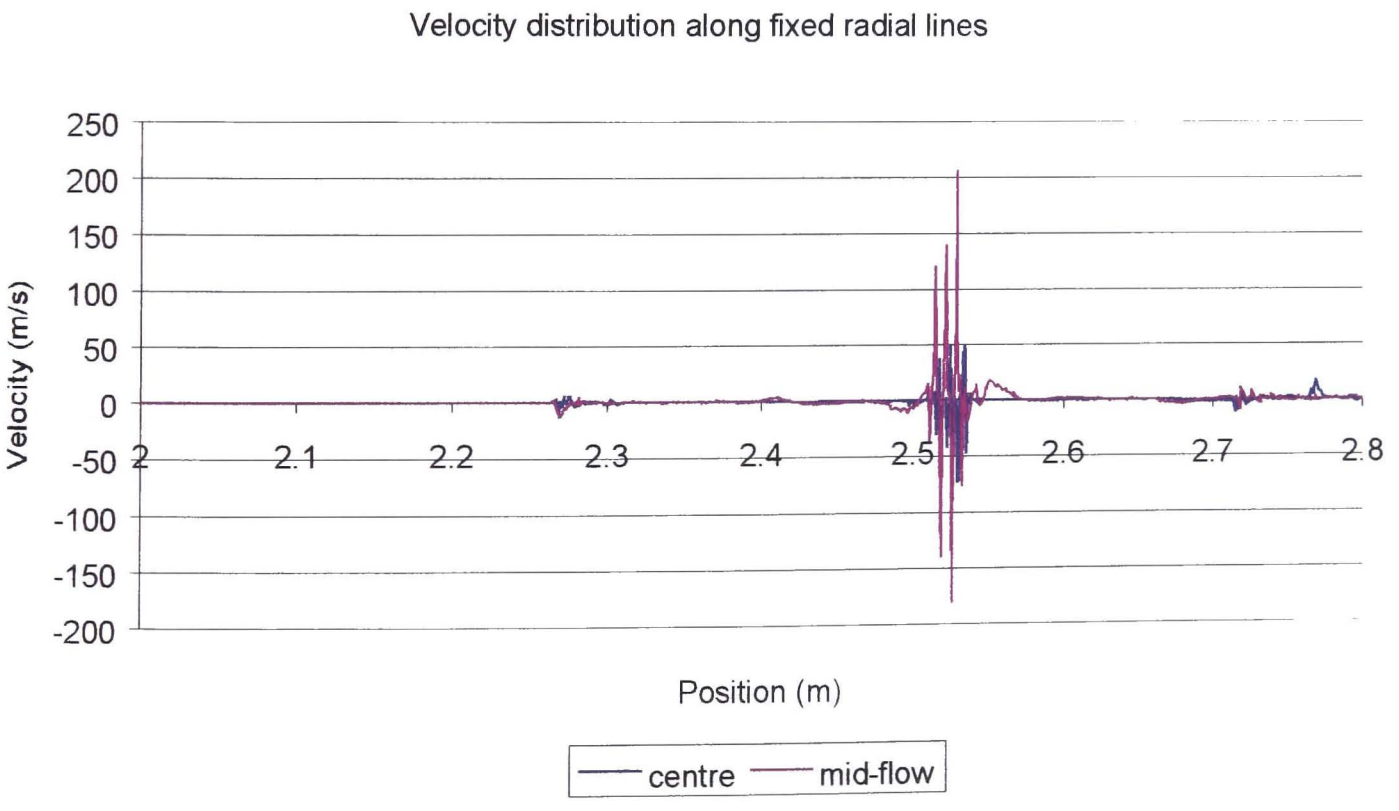

Figure 6.10 – Velocity distribution along a radial axis in the CFD shock tube.

6.7 *Discussion of experimental results and CFD simulations – Ceramic foam*

The sample 1 ceramic foam had a diameter of 50 mm making it smaller than the internal diameter of the shock tube – 55 mm. To securely hold the ceramic foam in place, a smaller fixture was designed and manufactured. This further restricted the area of the sample open to the incident shock wave. Thus, the results obtained for the sample 1 tests are different to that from the other five samples, especially when comparing those with a similar porosity value. (See Figure 5.13). This figure shows the remains of ceramic foam that has disintegrated, usually after the fifth/sixth consecutive shock wave has impinged upon it. This phenomenon was not experienced with the remainder of the ceramic foam samples, meaning that the sample 1 ceramic foam was not as strong. The other samples, having bigger diameters than the internal diameter of the shock tube did not suffer from failure and were securely held in place by their respective fixtures. Figure 6.11 shows the incident, reflected, and transmitted pressures from the CFD simulation of sample 1.

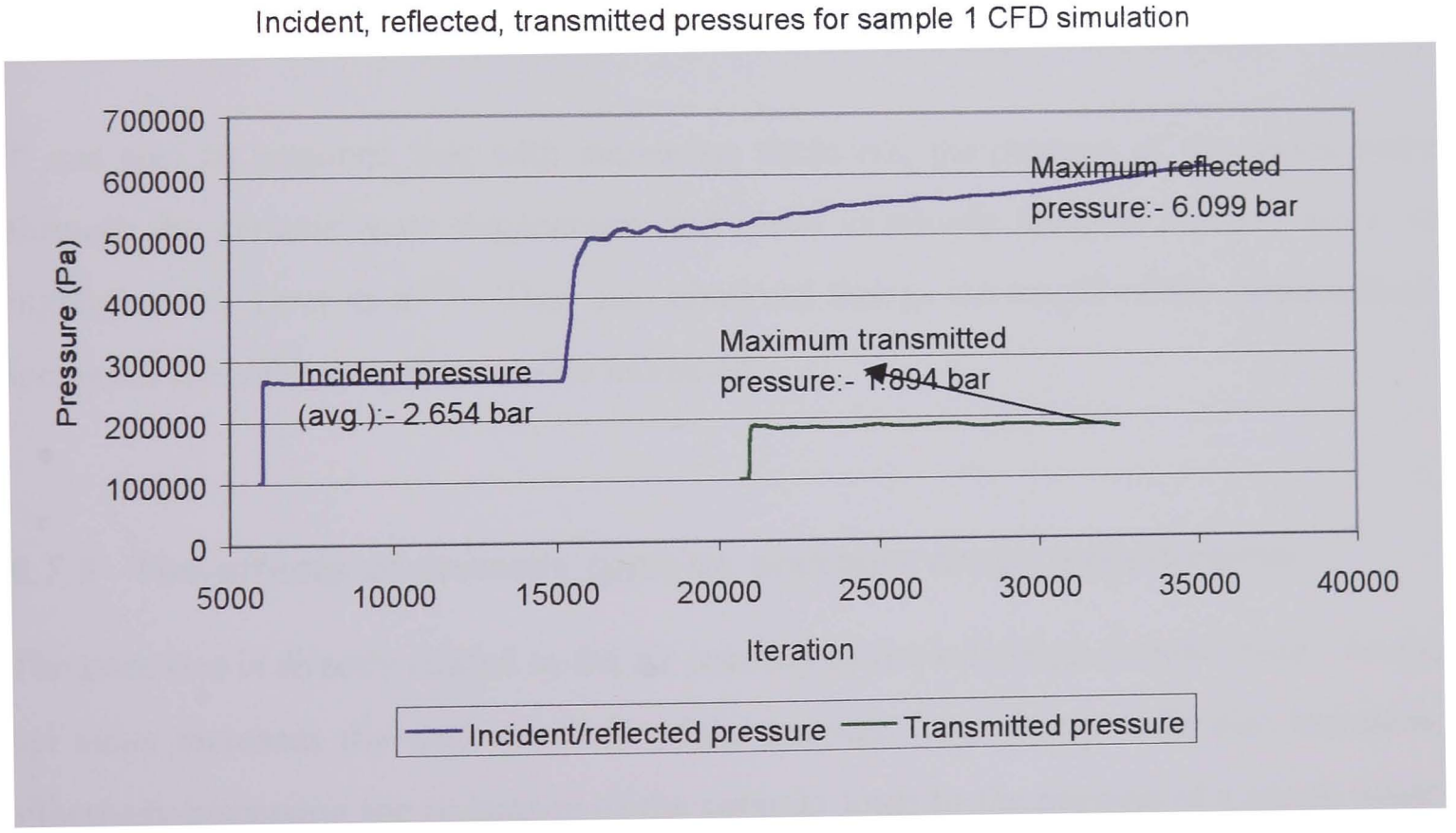

Figure 6.11 – CFD simulations results from sample 1.

6.7.1 Ceramic foam thickness and pressure drop (experimental)

The shock wave travelling through the ceramic foam has to travel a greater distance as the thickness of the ceramic foam increases. Thus, the thicker the ceramic foam, the greater the pressure attenuation. In terms of the thickness value, there were two samples of ceramic foams tested, 20 mm, and 25 mm. Sample 1 and sample 4 had the same ppi value but different thickness, thus care must be taken in the analysis of the effect of thickness on the pressure drop. However, samples 3 and 6 had different thickness and the same porosity.

Assuming that the dissipation of the shock along the radial axis of the ceramic foam was insignificant, then the pressure drop is proportional to the thickness of the foam. Sample 3 being the thinner of the two samples transmits more of the incident shock wave. However, the reflected pressure magnitude is similar in both samples. Thus, it can be assumed that the ppi value of the ceramic foam and the area exposed to the incident shock wave dictates how much of the incident shock wave is reflected. [The effect of ppi value on the pressure change across the ceramic foam is discussed in the following section, 6.7.2]. Also, as the thickness increases from 20 mm to 25 mm, so the pressure drop increases but not in proportion to the increase in thickness which is 25%.

It can also be assumed that with increasing thickness, the passage of the shock wave through the ceramic foam degenerates and could eventually become a sound wave, as highlighted by Levy et al[91]. They also observed that as the length of the ceramic foam increased the reflected pressure also increased.

6.7.2 The effects of porosity (ppi) on pressure drop - experimental

The pore size is directly related to the air porosity of the individual ceramic foam. As the ppi value increases the web structure of the ceramic foam that is solid also increases, effectively increasing the resistance of the ceramic foam to the passage of a shock wave. This means that more of the incident shock wave will be reflected and less will be transmitted.

The experimental results for samples 2 and 3 show the reflected pressure to be similar in both cases. Based on the earlier assumption that the speed of the shock is such that very little of the incident shock wave is dissipated along the radial direction of the ceramic foam, such closeness in their pressure characteristics can be attributed to the following factor: -

- though having a lower ppi value (15 against 20), sample 2 has a greater thickness (25 mm against 20 mm) and thus this extra thickness provides more resistance to the flow of the shock wave.

Figure 6.12 shows a typical signal obtained from the pressure transducers fore and aft of the ceramic foam. This figure shows the reflected and transmitted pressures for a 10 ppi ceramic foam. The incident pressure is detected by the channel 2 and channel 0 pressure transducers briefly before the arrival of the reflected pressure. The channel 1 pressure transducer detects the transmitted pressure. From these results, as the ppi value increases more, the ceramic foam becomes more restrictive and the area open to the incident shock wave increases in density. Thus more of the incident wave will be reflected regardless of the thickness of the ceramic foam.

With sample 3 and sample 6 having the same ppi value but different thicknesses, the effect of the ceramic foam thickness on the pressure drop can be ascertained. The reflected pressure is similar in both cases. (See Table 6.9). The ppi value (when the diameters are the same) determines the magnitude of the reflected pressure. The transmitted pressure has a lower magnitude from the sample 6 experimental tests. Figure 6.13 shows the change in pressure across the ceramic foam for the experimental tests and the CFD simulations.

Having the same thickness but different porosity give a useful comparison between the experimental results for samples 4, 5, and 6. The experimental results show that as the porosity of the ceramic foam increases the pressure drop decreases and the reflected pressure increases. As the porosity value increases from 10 to 20, the transmitted pressure is of the order of 8%, and 6% between the 20 ppi sample 5 ceramic foam and

the 30 ppi sample 6 ceramic foam. With the porosity acting as resistance to flow, this behaviour is to be expected.

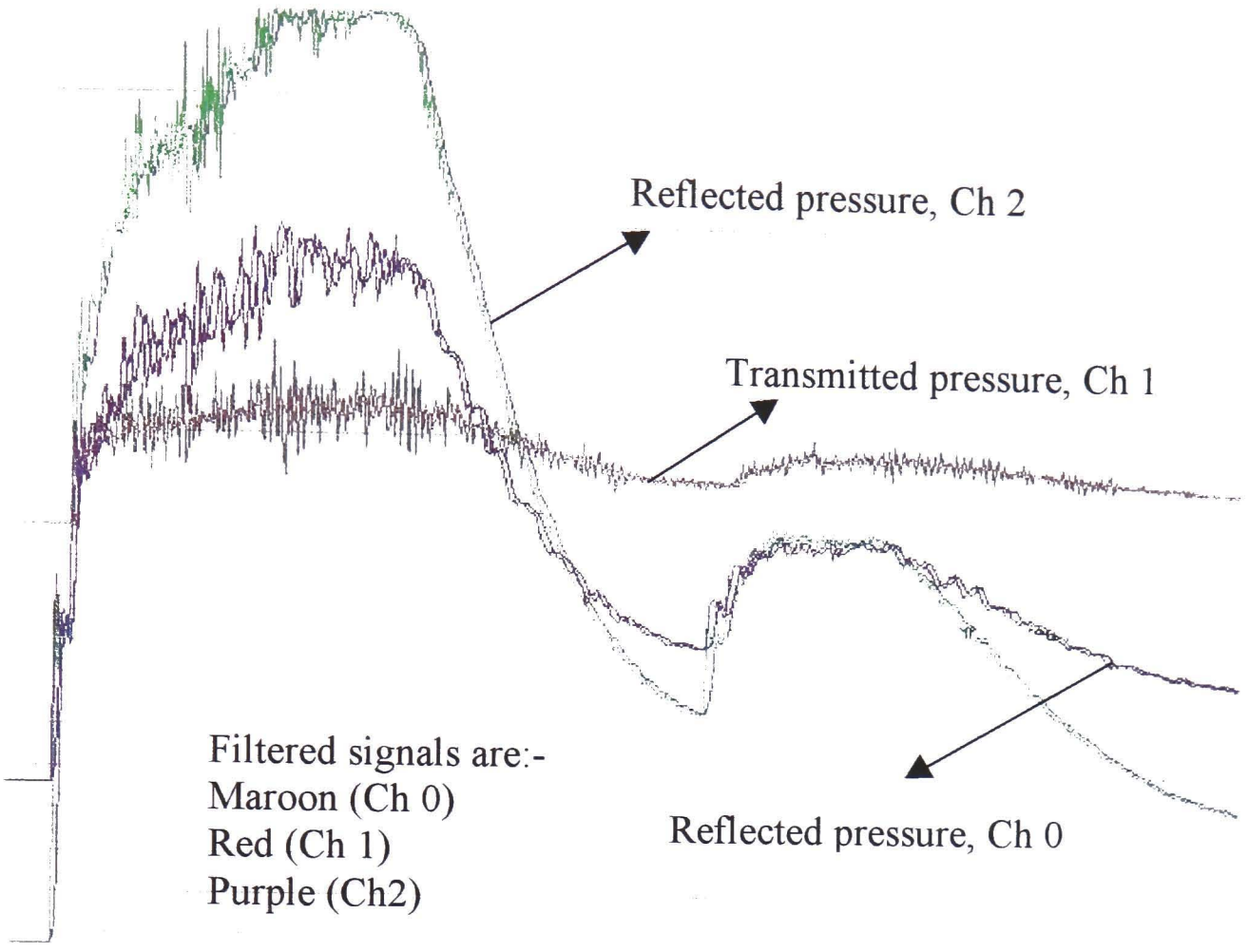

Figure 6.12 – Signal from the data acquisition software for a ceramic foam.

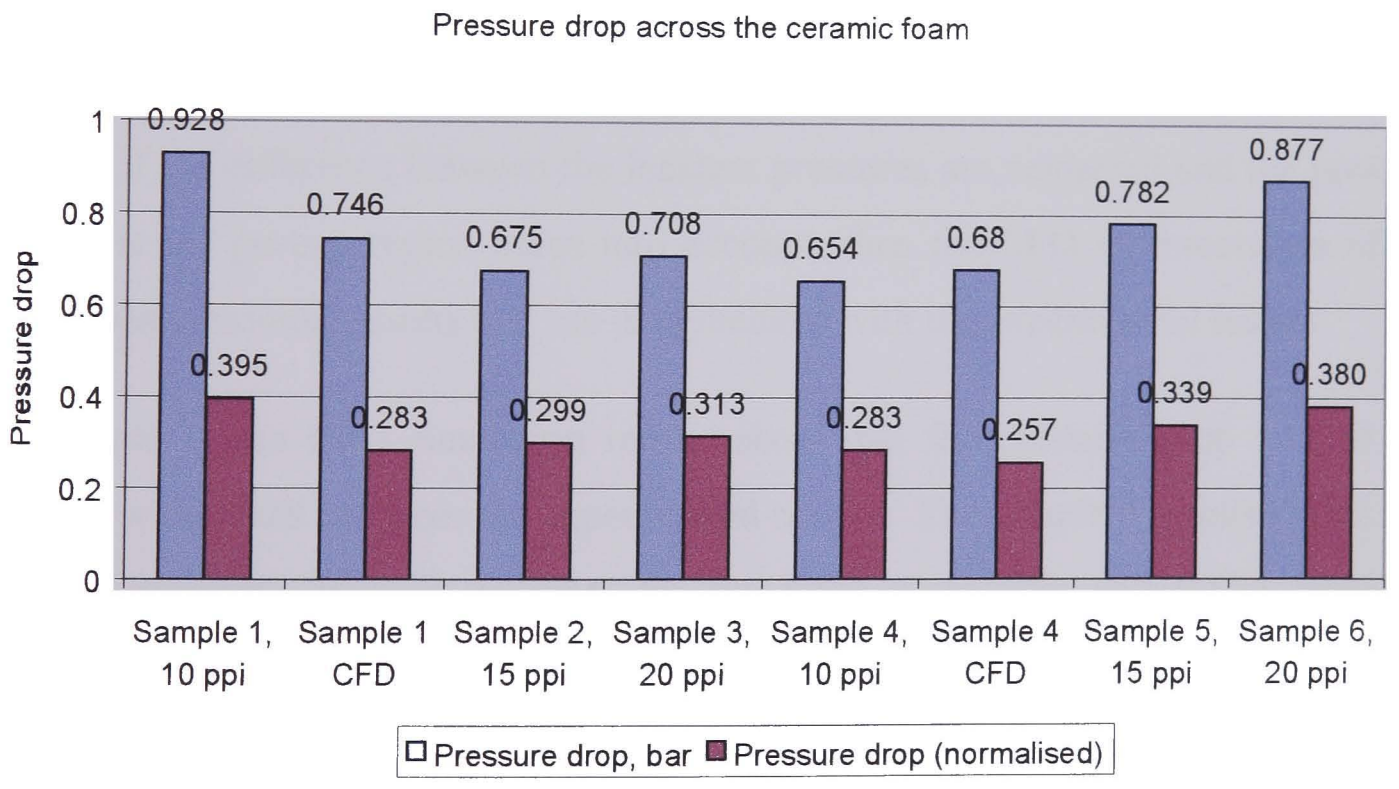

Figure 6.13 – Pressure drop across the ceramic foam – experimental and CFD simulations.

6.7.3 The CFD model of the ceramic foam

The discussions in this section are based on the CFD simulation tests conducted on the CFD model of the samples 1 and 4 ceramic foam. The differences between these two samples were in their exposure to the incident shock wave, and their thickness within the test section of the shock tube. Both models had a porosity of 10 ppi.

In each case, the ceramic foam was represented by a series of rings (when modelling the problem as axisymmetric) within the shock tube. This methodology was arrived at by a method described earlier in section 5.4.1. Figure 5.20 shows the layout of the obstructions with the shock tube for sample 1, Figure 5.21 shows that the fixture holding sample 4 in place did not intrude the shock tube – allowing the whole of the incident shock wave to impinge upon the sample.

As expected there is a difference in the incident pressure values between the experimental and CFD tests. This is due to the fact that certain assumptions made earlier for the CFD simulations may not be valid for the experimental tests.

Primarily,

- that the diaphragm is punctured instantaneously leading to the formation of a planar wave.

However, if the difference between the incident pressures are neglected and the pressure drop across the porous region taken into account, then the CFD representation of the ceramic foams produce results that are in agreement with the experimental results.

With sample 1, the CFD simulation results show that the pressure drop is 0.74 bar compared with 0.928 bar from the experimental results. The sample 4 results reveal that there is a pressure drop of 0.67 bar for the CFD simulation, and 0.654 from the experiments. An advantage of the CFD models is the ability to visualise the nature of the flow within the shock tube in the test region.

Figure 6.14 and Figure 6.15 show the velocity vectors for the flow around the obstructions within the shock tube.

The random nature of the flow through the porous region is shown in Figure 6.14. This shows the flow within the test section for the sample 1 CFD simulation. As the flow impinges upon the structure of the fixture securing the ceramic foam in place, the sudden reduction in area causes an increase in velocity and leads to a subsequent recirculation just upstream of the porous region. The shock wave eventually exits with a high velocity region just downstream of the porous region.

For the sample 4 CFD model simulations, the lack of any protrusions from the fixture securing the ceramic foam means that the whole of the incident shock wave impinges upon the ceramic foam. As such there is no recirculation of the flow as witnessed with the sample 1 CFD simulations. Also, the obstructions are not close to the outer wall and the symmetry axis, thus there is high velocity magnitudes in the radial direction of the shock tube.

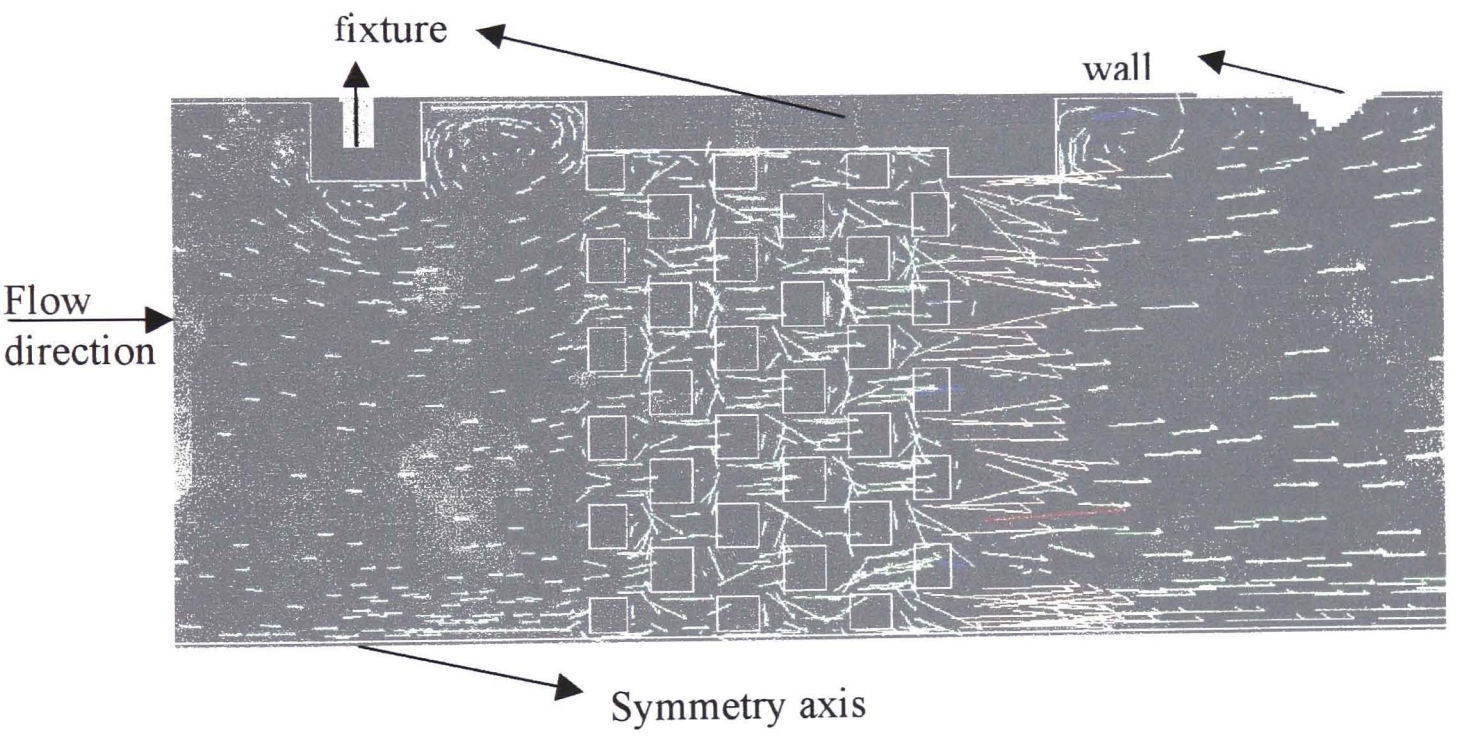

Figure 6.14 – Velocity vectors around the porous region – 68.3% porosity.

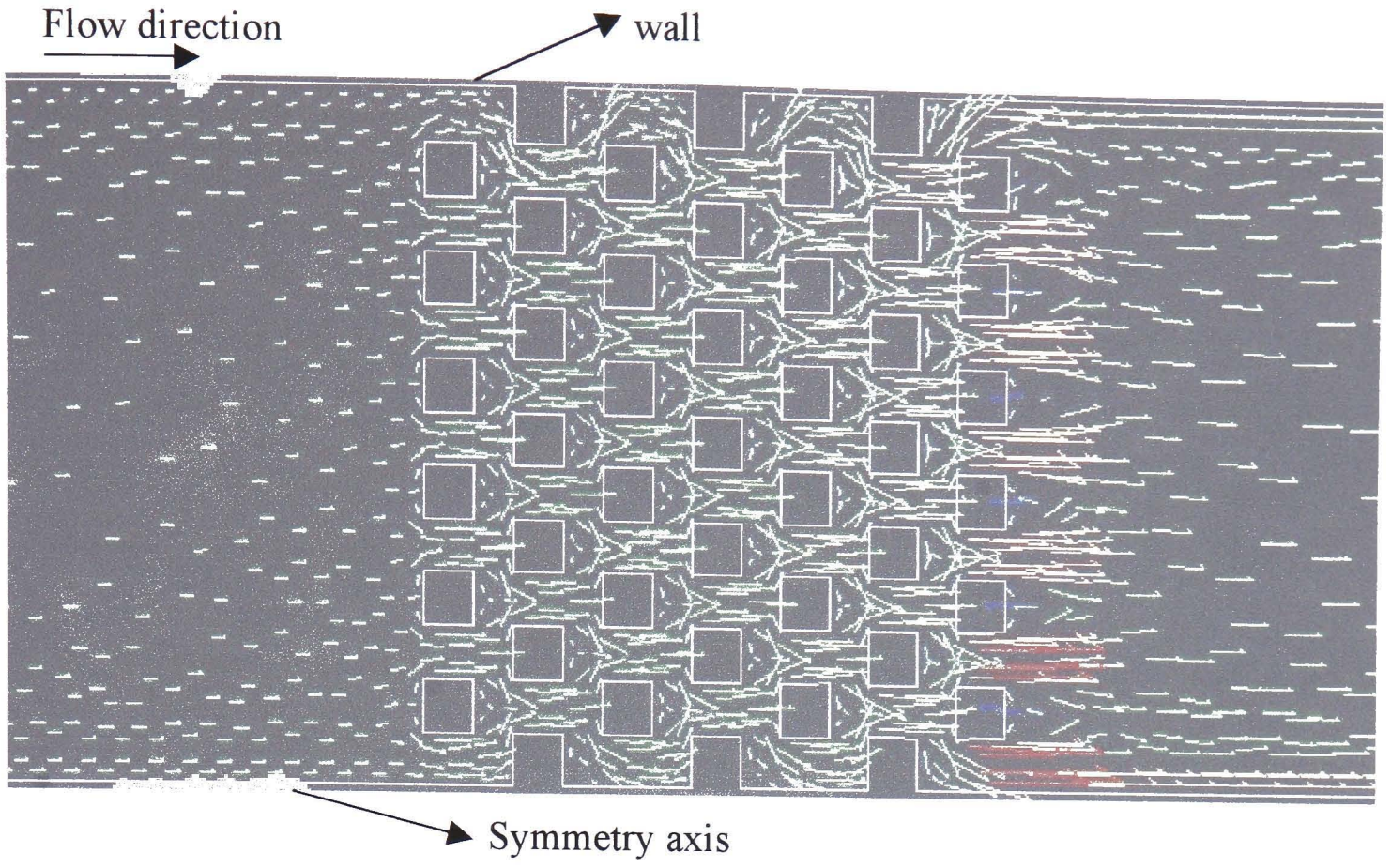

Figure 6.15 - Velocity vectors around the porous region for a Sample 4 ceramic foam CFD model.

Table 6.11 shows the results for the experimental tests and the CFD simulations of the sample 1 and sample 4 ceramic foams.

Table 6.11 – Pressure drop across the experimental and CFD ceramic foams.

	Sample 1			Sample 4	
	Experimental, bar	CFD, bar		Experimental, bar	CFD, bar
Pressure drop	0.928	0.74		0.654	0.670

6.7.4 The effect of changing the ceramic foam porosity – CFD simulation

One of the many advantages of CFD is the ability to make changes to geometry or boundary conditions easily and investigate the effects of such changes. Thus the effects of introduction a more restrictive CFD model of the ceramic foam was investigated by decreasing the porosity of the ceramic foam. This was done by increasing the size of the

obstructions within the test section of the shock tube in terms of their height (normal to the incident shock wave), and width (in line with the incident shock wave) The porosity values were randomly chosen and all the calculations were based on the sample 1 ceramic foam (and not sample 4).

The results discussed in this section are based on CFD simulations with no experimental tests for correlation. However, as the aim is to investigate the effect of restricting the flow through the test section of the CFD shock tube, the analysis are based on a comparison with the other air porosities.

Table 6.12 shows the results for the CFD model of the ceramic foam of sample 1 and the different configuration air porosity values that were simulated. For comparison purposes, the experimental result for the sample 1 ceramic foam (with 78.8% air porosity) is included.

The pressure drop from the experimental tests is 0.928 bar and that from the CFD simulations is 0.793 bar for the model that had a similar porosity for the test specimen.

As the air porosity was decreased, so the reflected pressure increased, and the transmitted decreased. Though for a 10% change in porosity, the reflected pressure increases by 4%, and the transmitted pressure decreases by almost 7%. The thickness of the CFD models were not altered for these series of simulations. The large transmitted pressure change between the 78.8% air porosity model and the 76.4% air porosity model could be attributed to the change in the obstructions within the porous region of the CFD model. The height of the obstructions (i.e. the side of the obstructions that is impinged by the incident shock wave) increases causing more of the incident to be reflected and less to be transmitted.

Table 6.12 – CFD and experimental ceramic foam results – Sample 1.

Configuration	Incident Pressure, bar	Reflected Pressure, bar	Transmitted Pressure, bar
Experimental	2.350	7.930	1.422
CFD 78.8% Air porosity	2.650	6.600	1.857
CFD 76.4% Air porosity	2.650	6.763	1.788
CFD 74.5% Air porosity	2.650	6.823	1.758
CFD 68.3% Air porosity	2.650	6.856	1.730

Figure 6.16 shows the reflected and transmitted pressure for the CFD models of the sample 1 ceramic foam at various air porosity values (c.f. Figure 6.3 which shows the reflected and transmitted pressures for the thin orifice plates). As the air porosity decreases (signifies an increasingly solid structure), the reflected pressures increases reaching an asymptotic value. Likewise, there is a similar behaviour for the transmitted pressure which decreases as the ceramic foam is made more solid by decreasing the air porosity value.

Figure 6.17 shows the contours of pressure for the CFD model of the ceramic foam with an air porosity of 78.8% - same value as sample 1. The figure shows that the shock wave has already impinged upon the porous region and that it has been both reflected and transmitted. Just downstream of the porous region is a region of very low pressure that gradually increases in magnitude. The low pressure region is due to the high velocity jets that exit the porous region. For this model the obstructions all have the same size, the reflected pressure is approximately double that of the incident pressure and the transmitted pressure around 1.9 bar.

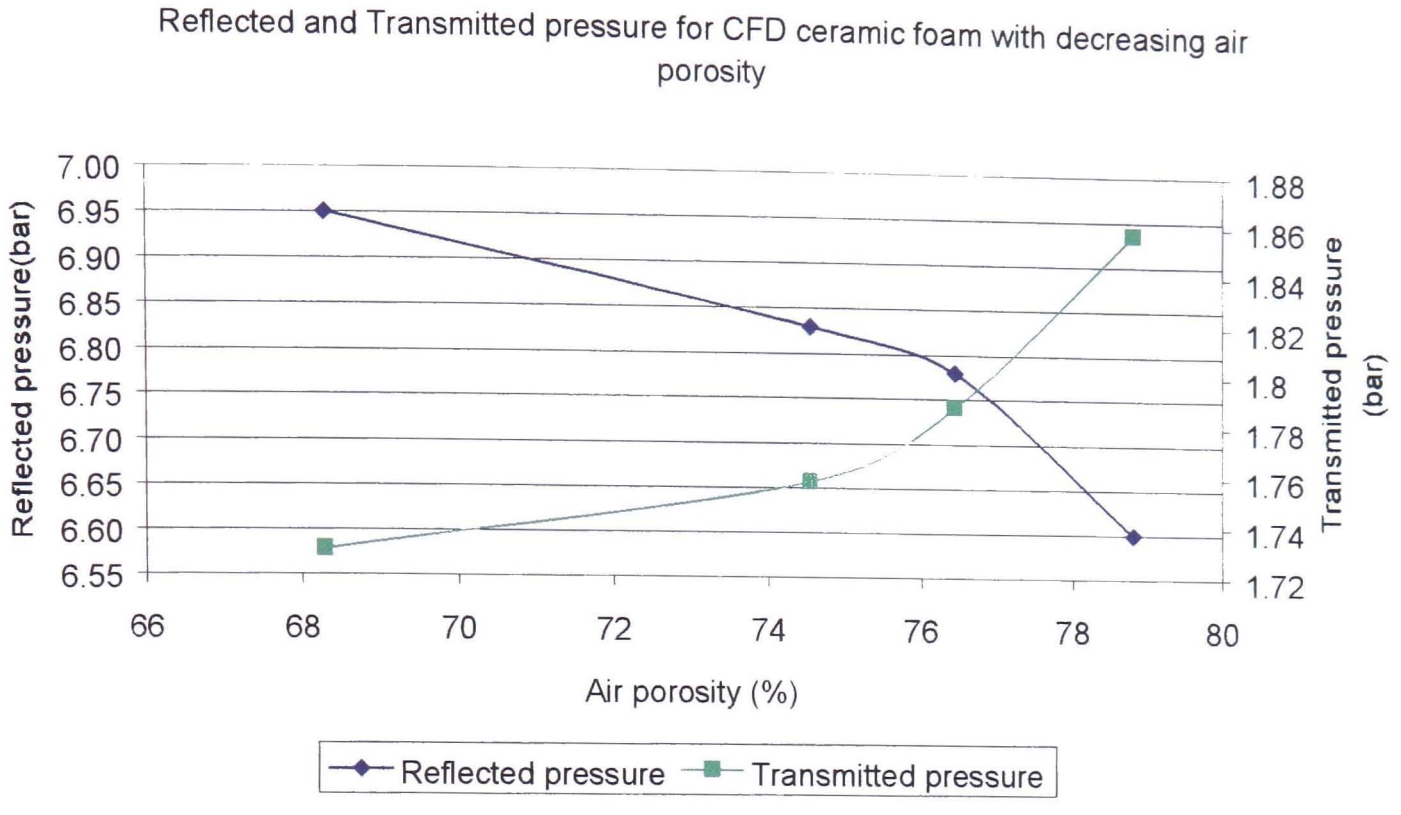

Figure 6.16 – Incident pressure and transmitted pressure at various air porosities for the CFD model of the ceramic foam – sample 1.

Figure 6.18 shows plot of the pressure distribution with the CFD shock tube some time after the diaphragm was punctured. The pressure distribution was taken along three sections of the shock tube to show any differences between the flow within the shock tube. This figure shows the position of the reflected and transmitted pressure at a point in time. The reflected shock wave in time decreases in magnitude as does the transmitted pressure. The plot also reveals that the flow within the shock tube changes very little across the cross-section of the shock tube.

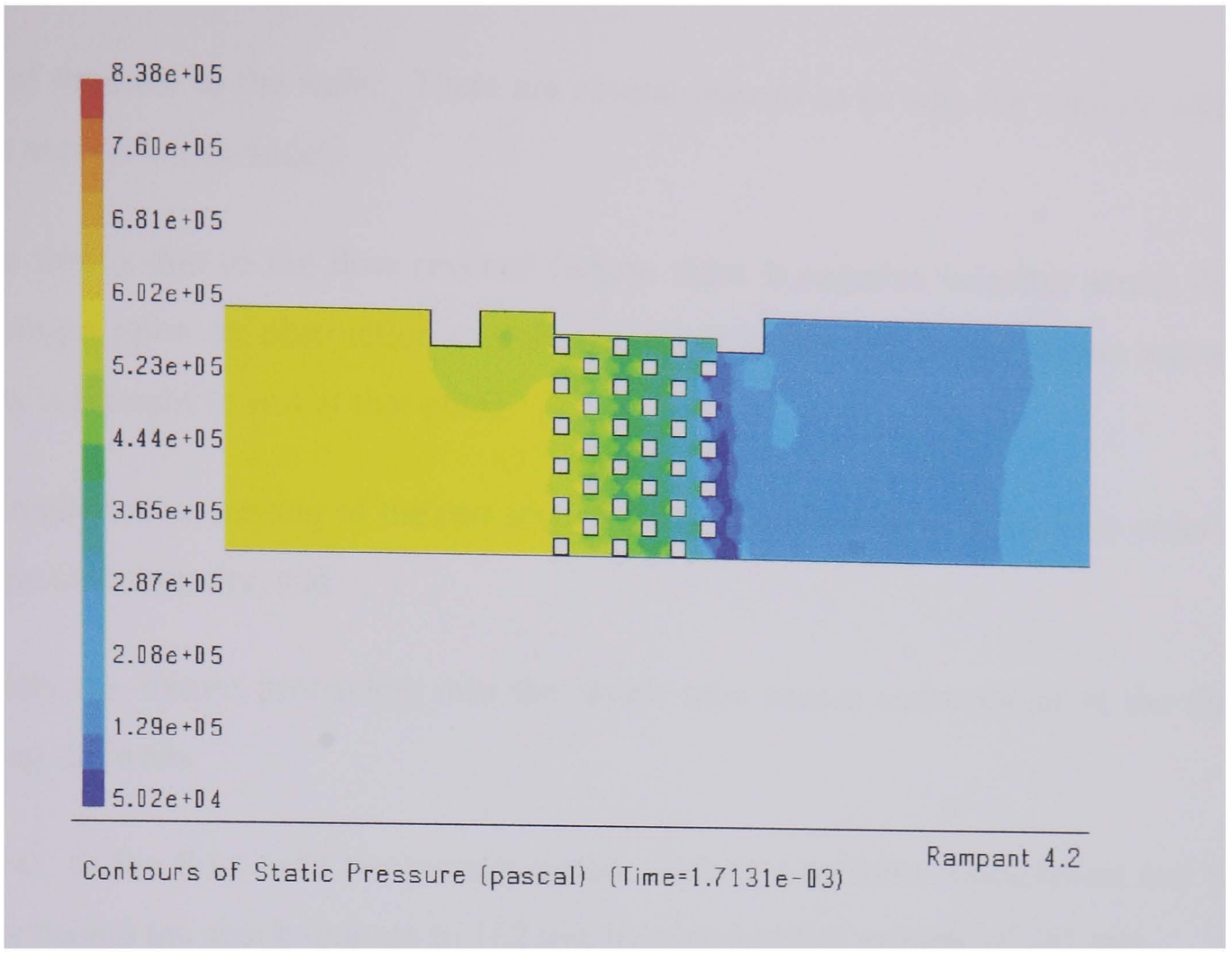

78.8% air porosity

Figure 6.17 – Pressure contours around the porous region – 78.8% air porosity.

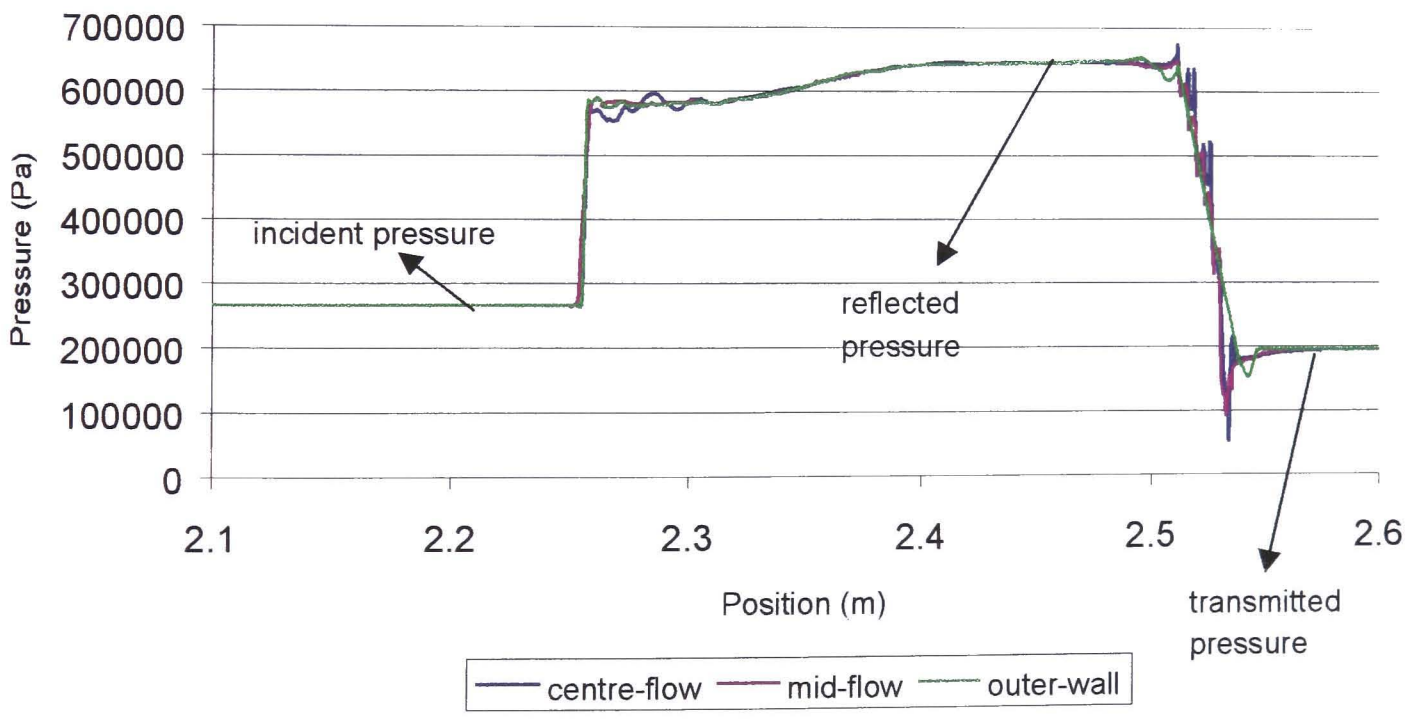

Figure 6.18 – Pressure history for a 78.8% air porosity CFD simulation.

Figure 6.19 shows the velocity distribution along the shock tube for the 78.8% air porosity CFD ceramic foam. Here, the distribution within the shock tube varies from the

centre of the tube to the walls. There are several reasons as to why the velocity within the test section varies widely.

- The first is due to the flow reversal (where there is negative velocity) as the flow impinges upon an obstruction (see Figure 6.14) within the porous region and the flow is brought to rest at that point,

- secondly the narrowing of the test section causes the velocity to increase in order to maintain continuity, and

- thirdly the fixture protruding into the shock tube causes recirculation of the flow along the walls.

However, as the flow exits the porous region, there is a uniform reattachment and the velocity behind the shock reduces to 162 m/s from an incident velocity of 261 m/s.

Figure 6.20 shows the contours of velocity for the 78.8% air porosity CFD ceramic foam. The high velocity areas shown in Figure 6.19 appear as the red regions just downstream of the last obstructions in the test section of the CFD shock tube. As the shock wave travels through the velocity increases until it reaches a peak value just downstream of the last obstructions. There is some recirculation along the walls of the shock tube shown by the blue regions upstream and downstream.

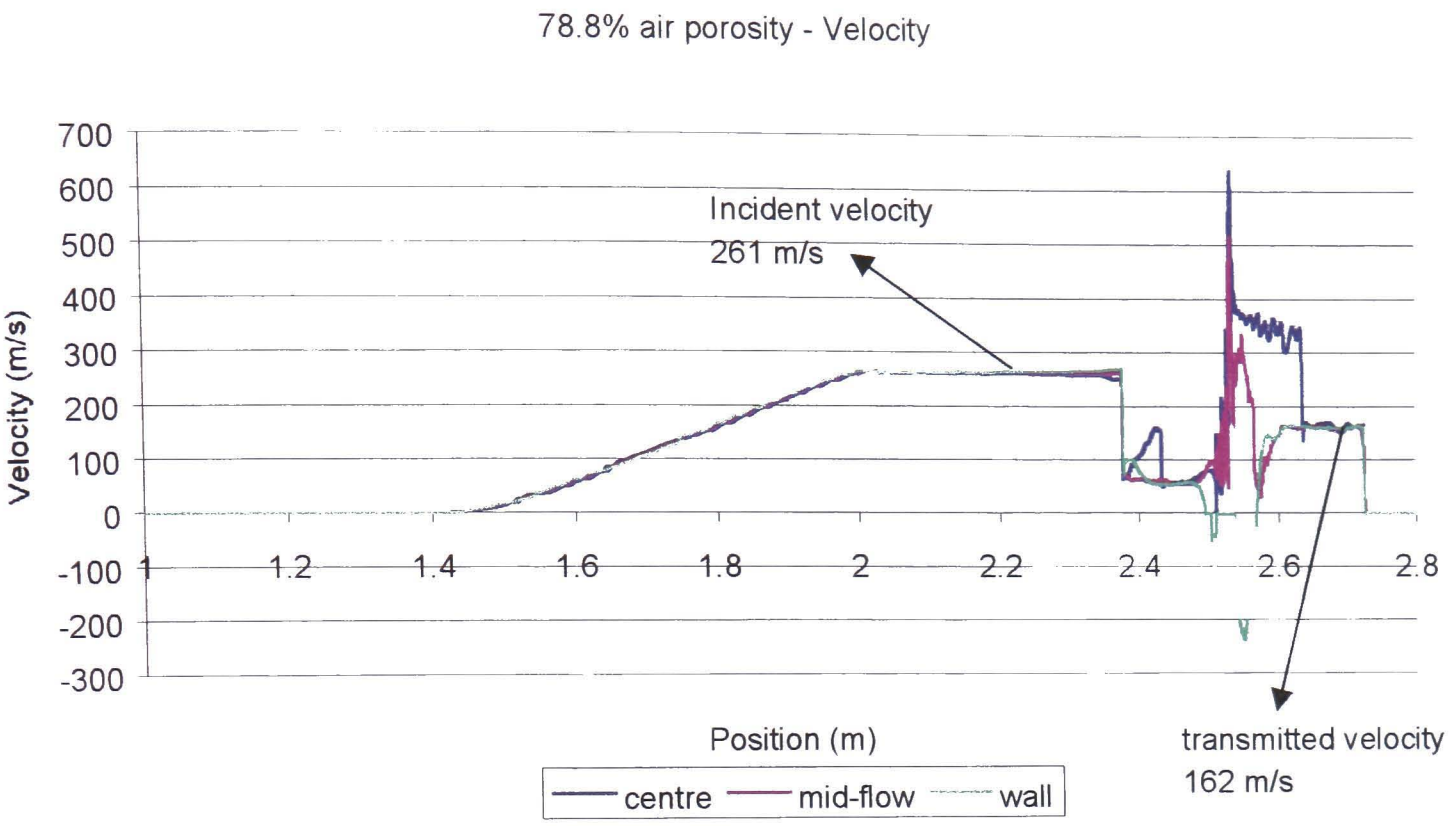

Figure 6.19 – Velocity history for a 78.8% air porosity CFD simulation.

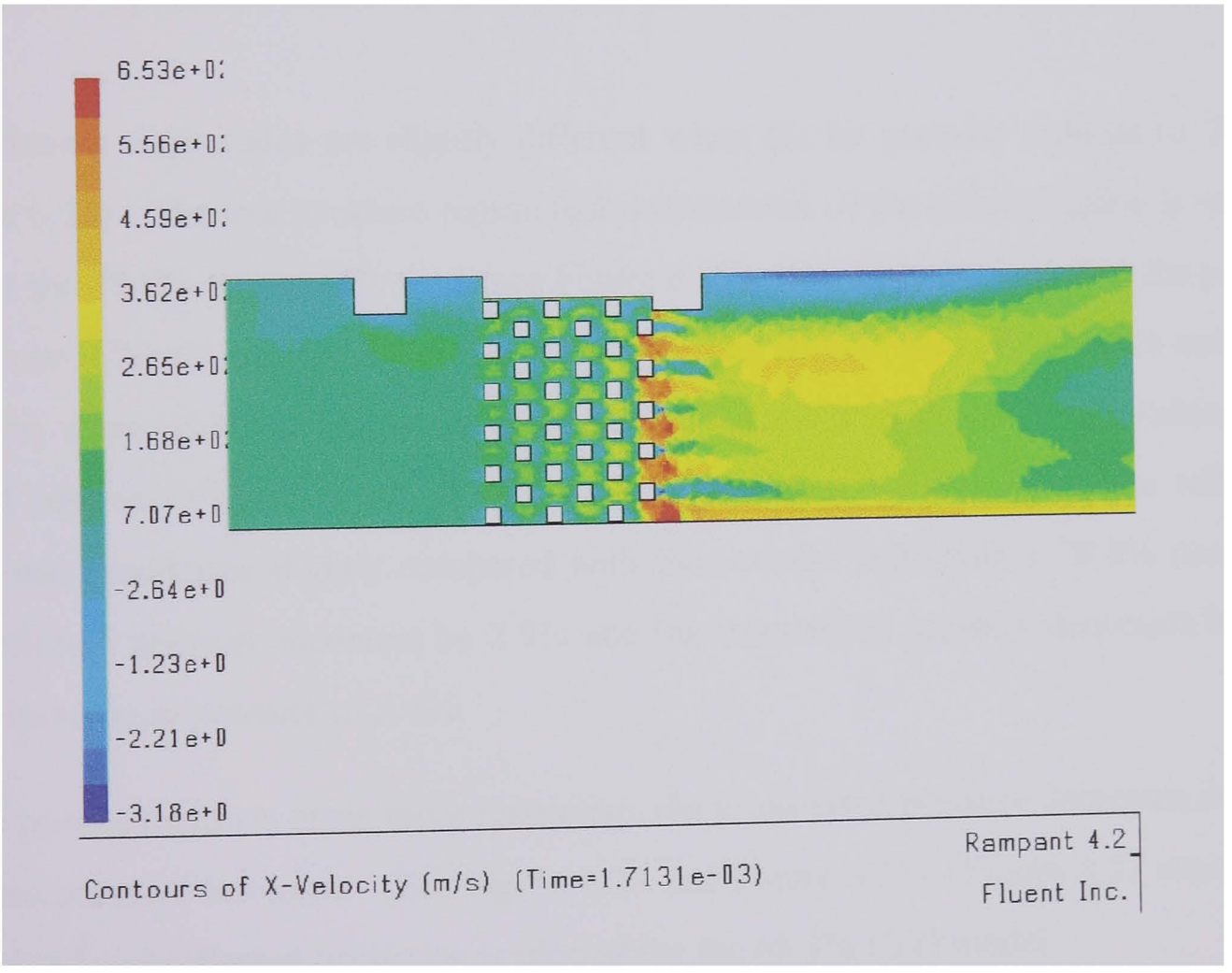

Figure 6.20 – Velocity contours around the porous region – 78.8% air porosity.

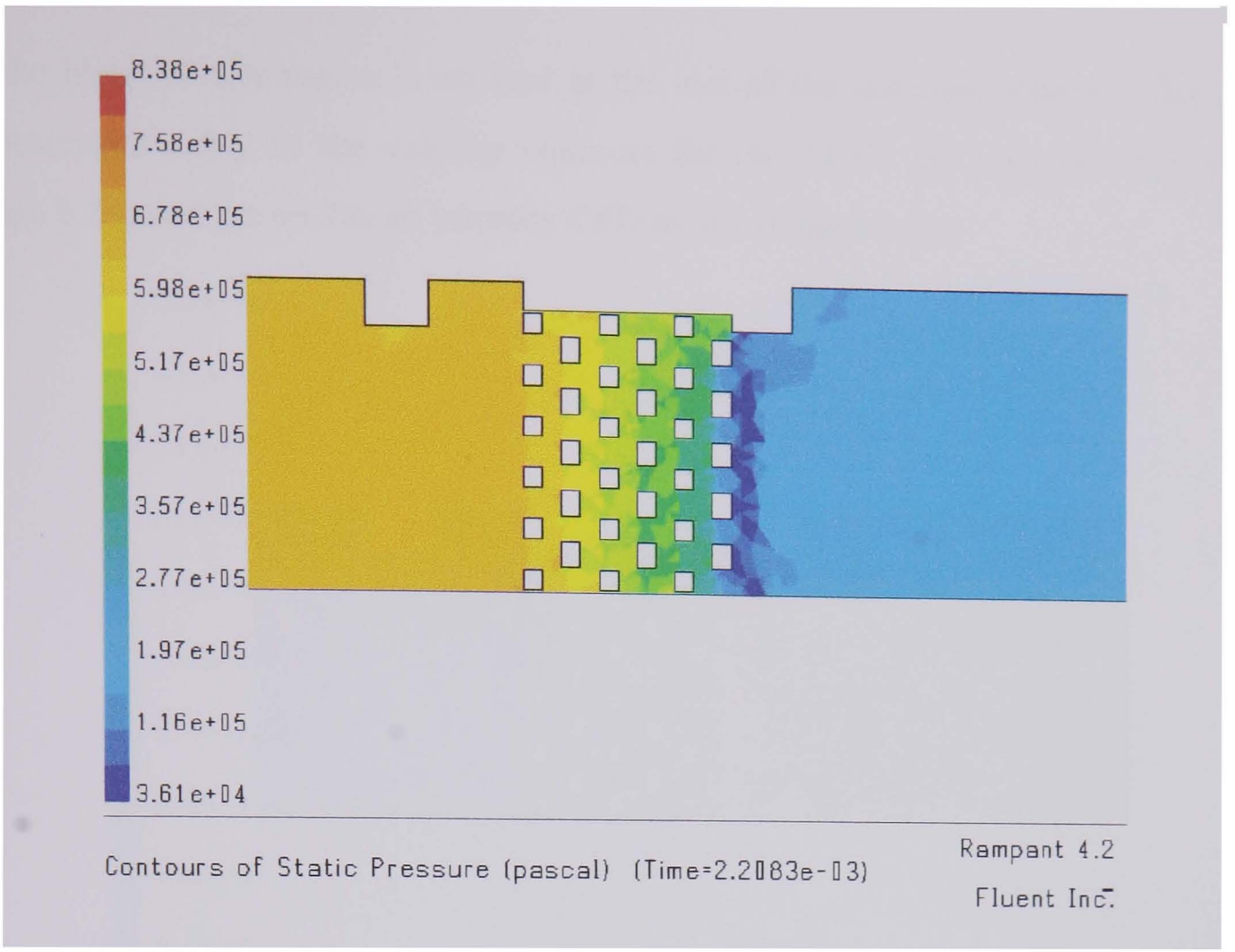

Figure 6.21 - Pressure contours around the porous region – 76.4% air porosity.

The pressure magnitudes are slightly different when the air porosity reduces to 76.4% (Figure 6.21). The low pressure region just downstream of the porous region is akin to that for the 78.8% air porosity tests (see Figure 6.17). The rings representing the porous region are different and are not uniform in size. The second, fourth, and sixth columns have the same width as the other obstructions but different height. By making the second column series of obstructions slightly bigger than the first series, the reflected shock wave increases slightly compared with the ceramic foam with a 78.8% porosity. The reflected pressure increases by 2.5% and the transmitted pressure decreases by 4% for an increase in porosity of 2.4%.

As the porous region is made more restrictive, the transmitted pressure decreases and the reflected pressure increases. (See Figure 6.23 and Figure 6.25). Figure 6.27 shows the transmitted and reflected pressures as plotted for the 68.3% CFD model.

The contours of velocity for the 76.4% air porosity CFD model (Figure 6.22) exhibit the same characteristics as that for the 78.8% air porosity model. The changes in peak values are slight. There is recirculation just upstream and downstream of the test section

and the high velocity region is situated at the end of the last obstructions. The same characteristics apply to the velocity contours for the 74.5% air porosity CFD model (Figure 6.24) and the 68.3% air porosity CFD model (Figure 6.26).

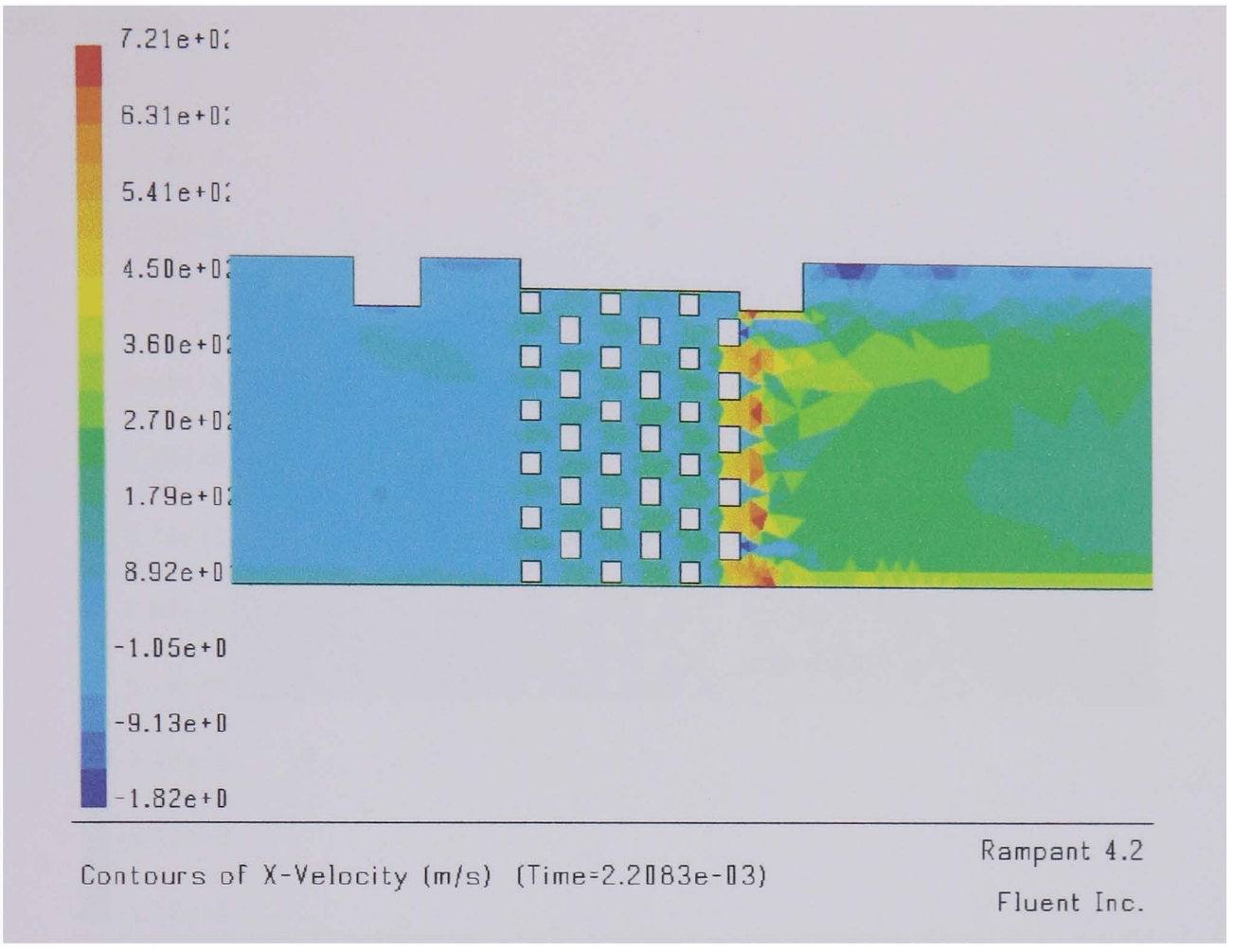

Figure 6.22 - Velocity contours around the porous region – 76.4% air porosity.

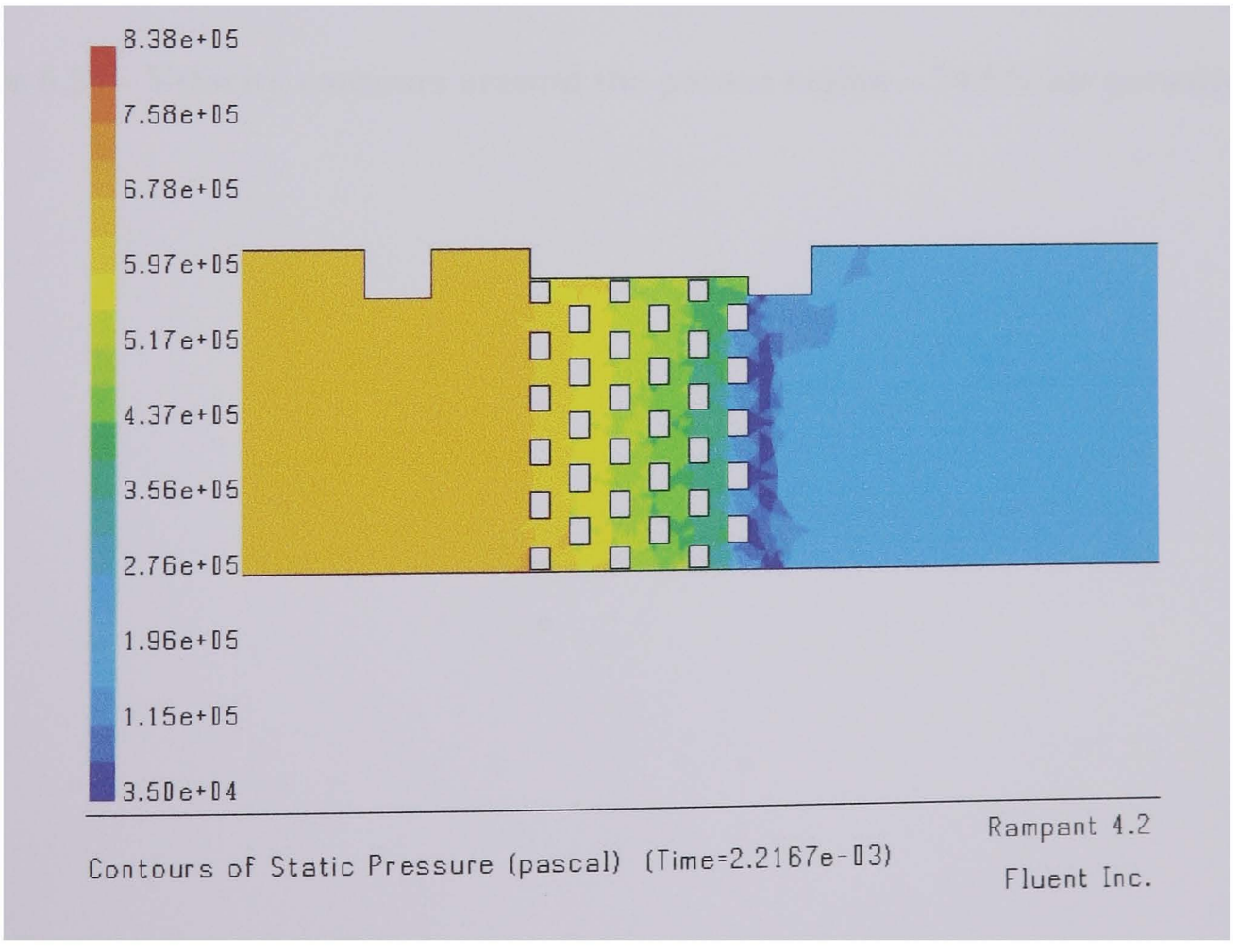

Figure 6.23 - Pressure contours around the porous region – 74.5% air porosity.

The pressure decrease through the test section is clearly visible. The high pressure region upstream of the test section is the pressure magnitude behind the reflected shock wave, whereas the transmitted wave magnitude is shown as the region just downstream of the test section.

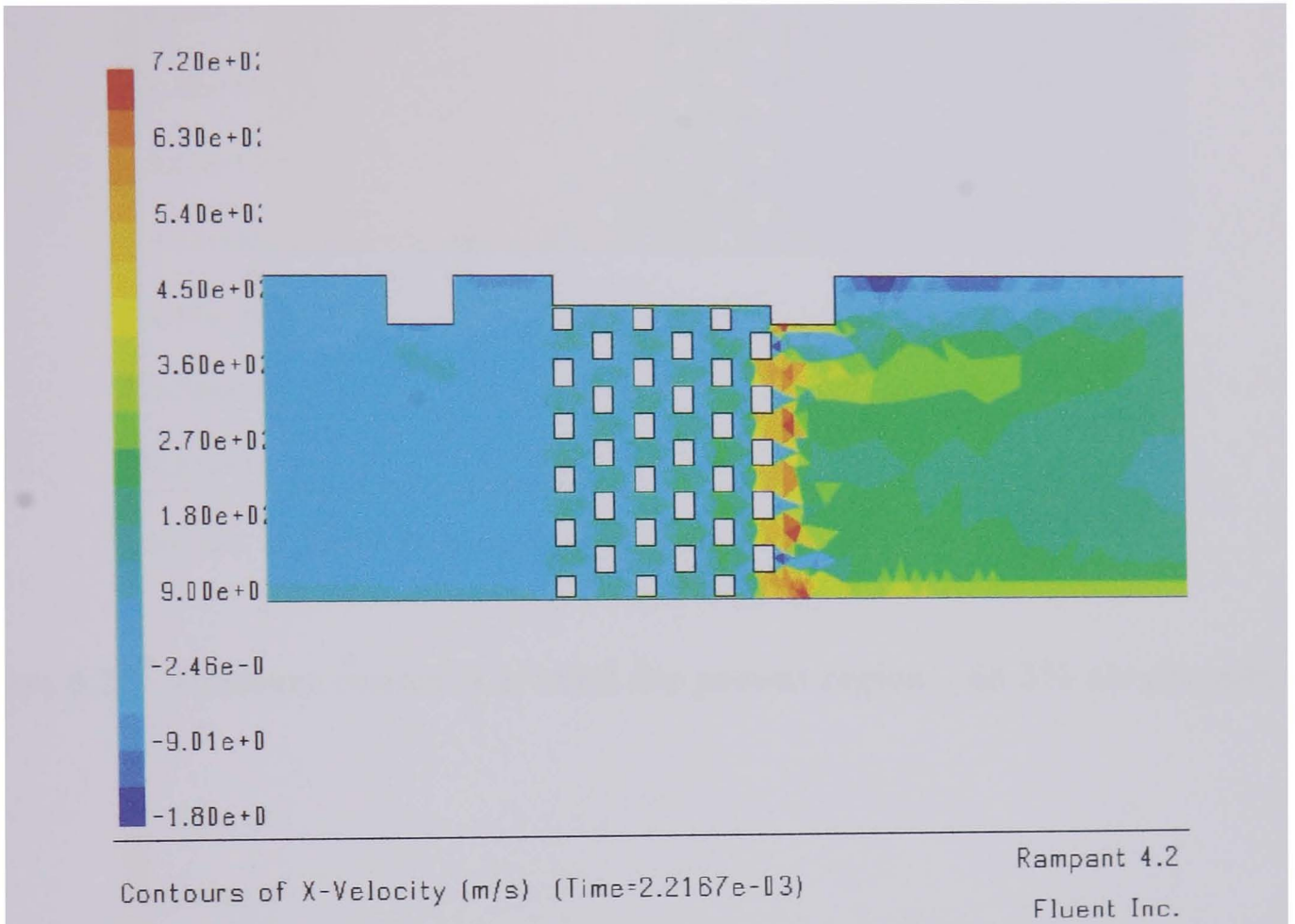

Figure 6.24 - Velocity contours around the porous region – 74.5% air porosity.

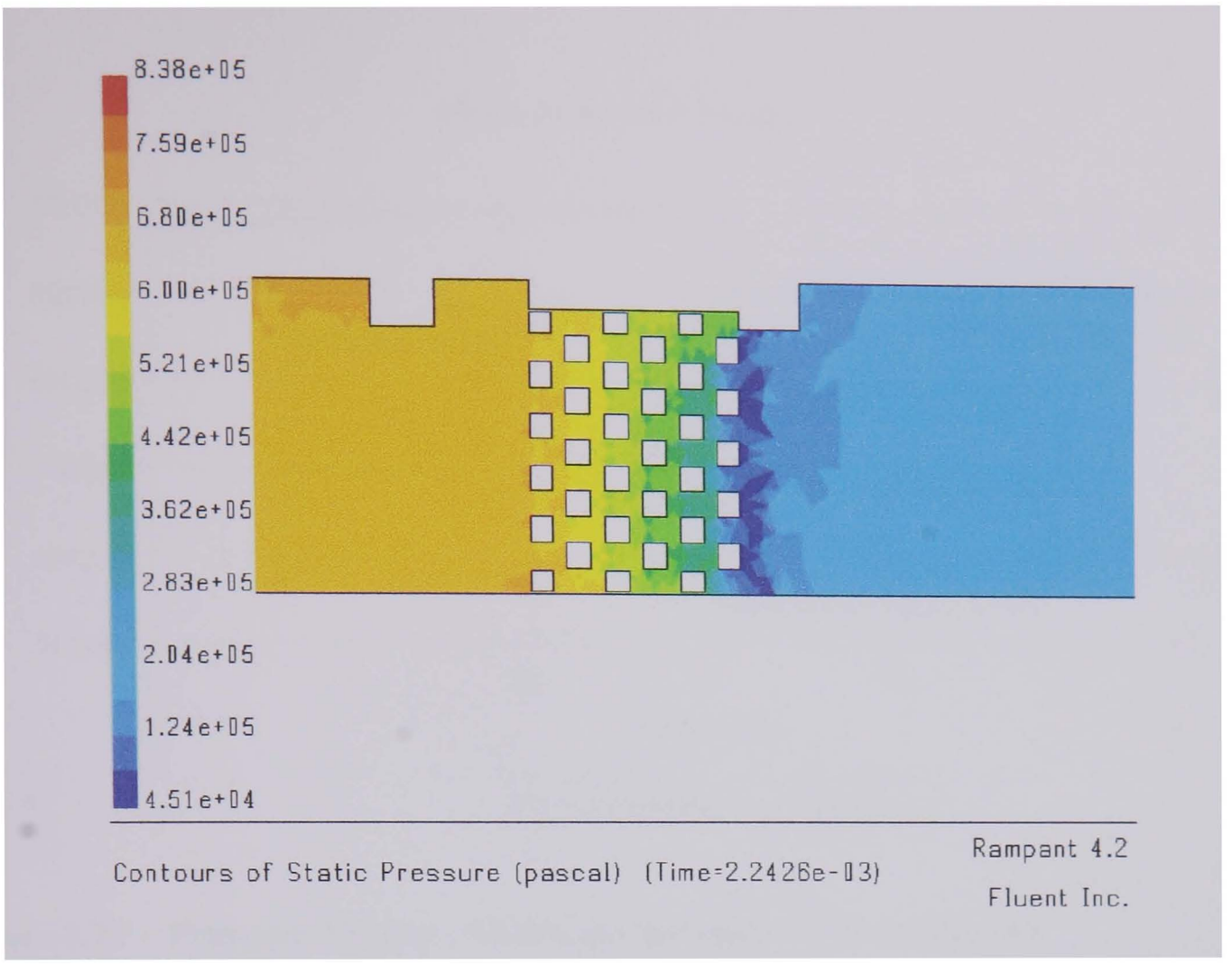

Figure 6.25 - Pressure contours around the porous region – 68.3% air porosity.

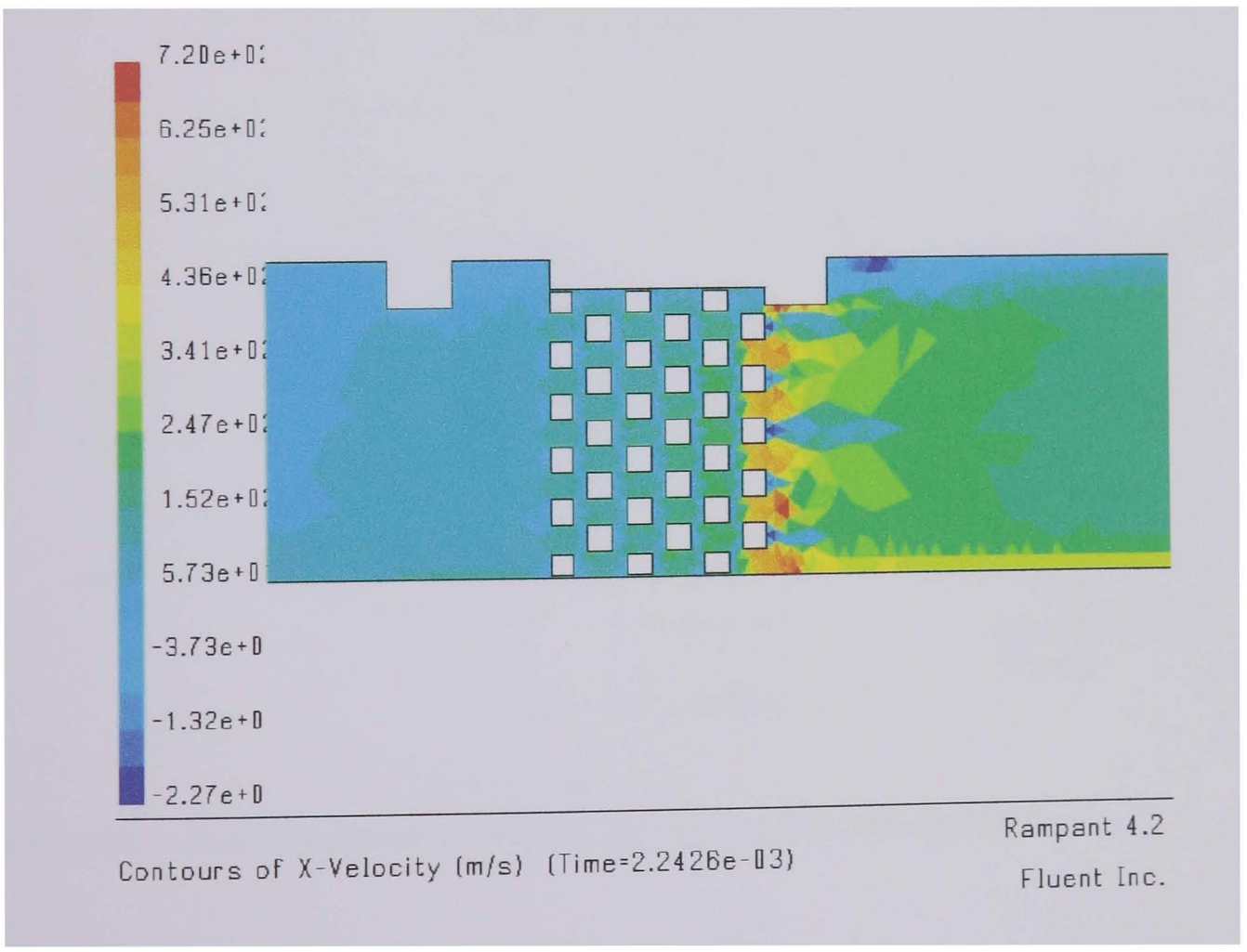

Figure 6.26 - Velocity contours around the porous region – 68.3% air porosity.

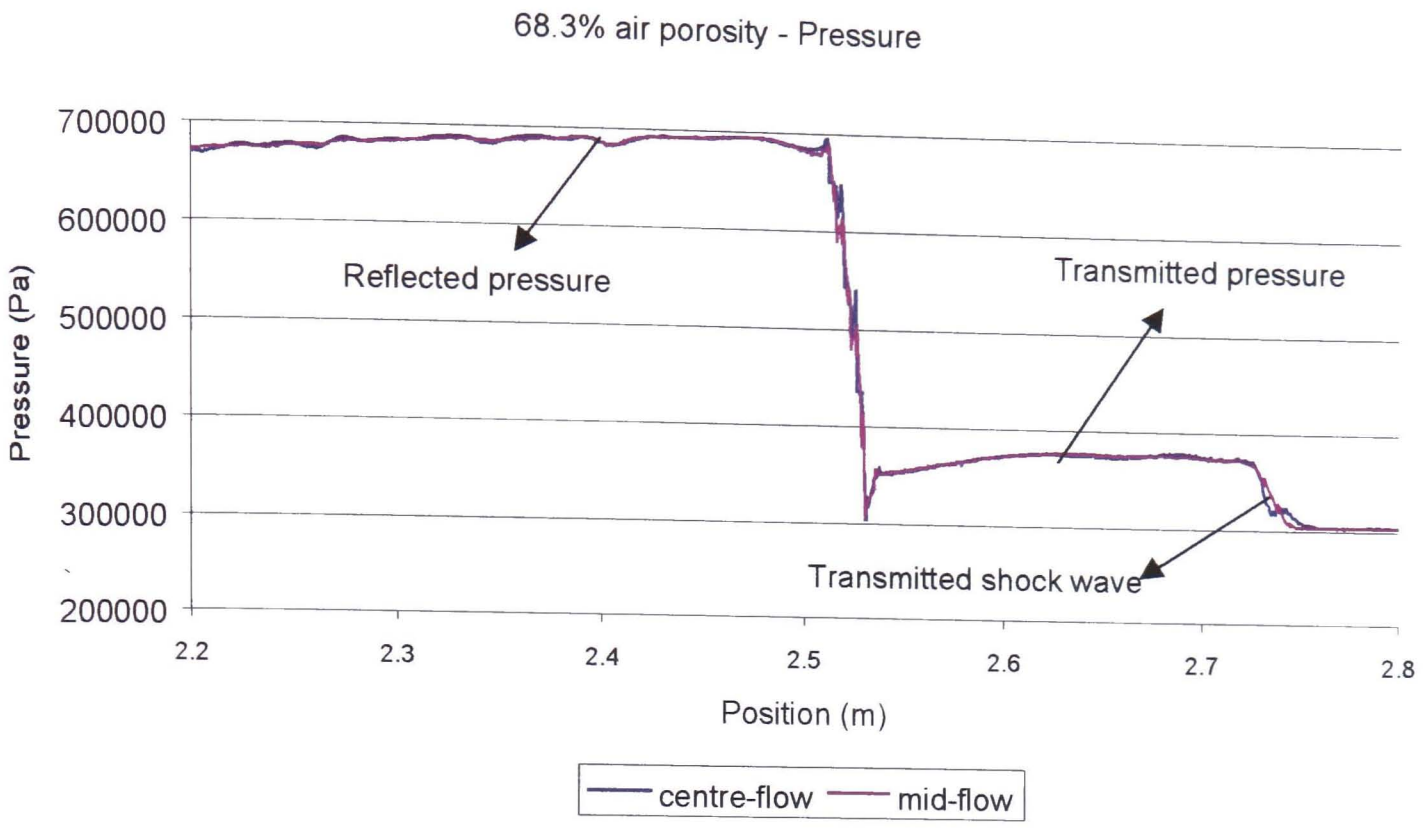

Figure 6.27 - Pressure history - 68.3% air porosity CFD simulation.

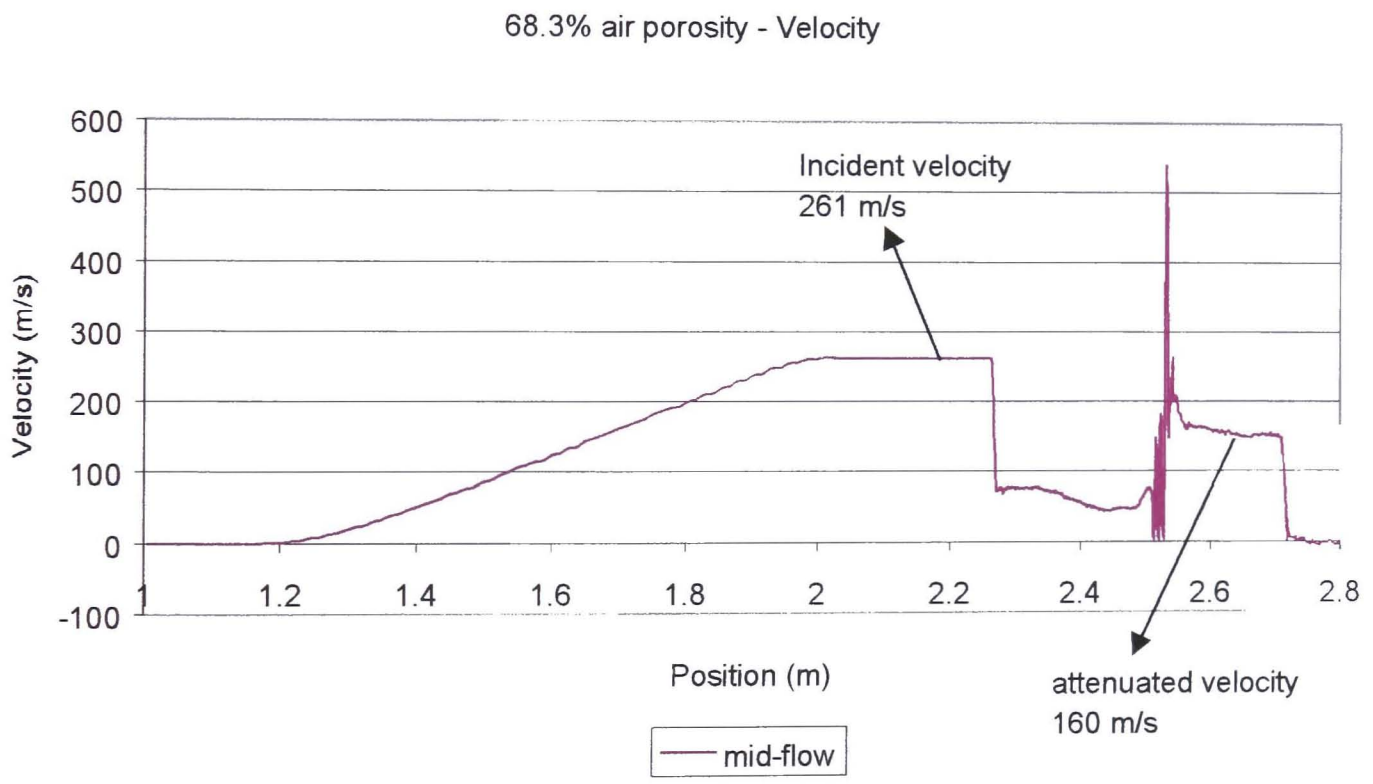

Figure 6.28 – Velocity history - 68.3% porosity CFD simulation.

Figure 6.28 shows the velocity distribution with the CFD shock tube with a 68.3% air porosity model. Within the porous region, there is a large variation in velocity as the shock wave negotiates the obstructions within the region as well as the volume decrease.

This causes the flow behind the shock to increase in velocity. Also, the obstructions bring part of the shock wave to a halt, as well as reverse the flow of the shock wave. However, downstream of the porous region there is reattachment and the flow behind the shock reduces to a magnitude of 160 m/s from an incident velocity of 261 m/s.

6.7.5 Comparison between the orifice plate tests and the ceramic foam

The object of the single and multiple orifice plate tests was to provide a useful means of correlating the results from the ceramic foam experiments with equivalent or similar orifice plate test results. It is hoped that as different configurations of the ceramic foam are tested, a database of comparison tables would help designers to understand the characteristics of ceramic foam as there are numerous published data on orifice plates.

The ceramic foam test results showing the pressure drop (taking into account the various incident pressures) are shown in the Table 6.13. The table shows that between 30% and 40% of the incident shock wave is dissipated through the ceramic foam.

Table 6.13 – Pressure drop across the ceramic foams.

Ceramic Foam	Pressure drop across the ceramic foam, bar	Pressure drop as a percentage of the incident pressure
Sample 1, 10 ppi	0.928	39
Sample 2, 15 ppi	0.678	30
Sample 3, 20 ppi	0.708	31
Sample 4, 10 ppi	0.654	28
Sample 5, 15ppi	0.782	34
Sample 6, 20ppi	0.877	38

The high pressure drop (from the experimental tests) across the sample 1 ceramic foam can be attributed to the small diameter of the sample and the fixture securing the ceramic foam to the shock tube. Due to the small diameter of the ceramic foam, the fixture protruded the shock tube, thereby acting as a solid obstruction from which the incident

shock wave could reflect. Comparison with the experimental data from Figure 6.6 show that for samples 2 and 3, the pressure drop across the ceramic foam is equivalent to that from an orifice plate that has a blockage area (BA) of close to 70%.

The air porosity of the ceramic foam is in the region of 80% meaning that 20% of the ceramic foam is solid and the rest is filled with air. This would mean that the ceramic foam should have characteristics similar to that from an orifice plate that was 20% blocked. However such a hypothesis fails to recognise that unlike the thin orifice plate which has a hole that allows the passage of some of the shock wave, the ceramic foam has a uniform distribution along its entire diameter as well as a greater thickness. Thus the whole of the shock wave impinges upon it and has to negotiate its passage through a greater distance and a series of small obstructions that form the structure of the ceramic foam, before exiting into the downstream section of the shock tube. The orifice plate had a thickness of 2 mm.

Table 6.14 – Normalised reflected and transmitted pressures for all test specimen.

Blockage Area/Ceramic foam	Normalised Reflected Pressure	Normalised Transmitted Pressure
Orifice plate 50%	2.270	0.862
Orifice plate 60%	2.543	0.771
Orifice plate 70%	2.893	0.698
Orifice plate 80%	3.306	0.580
Sample 1, 10 ppi	2.425	0.717
Sample 2, 15 ppi	2.552	0.661
Sample 3, 20 ppi	2.614	0.620
Sample 4, 10 ppi	3.374	0.605
Sample 5, 15 ppi	2.767	0.701
Sample 6, 20 ppi	2.711	0.687

Figure 6.29 shows the results for the ceramic foam and the orifice plates tested. It is a graphical representation of the data in Table 6.14. The experimental test results are shown here for comparison purposes. Also, the data is normalised using the incident pressure in each test. Thus, the reflected pressure values are greater than unity and the transmitted pressure values are less than unity.

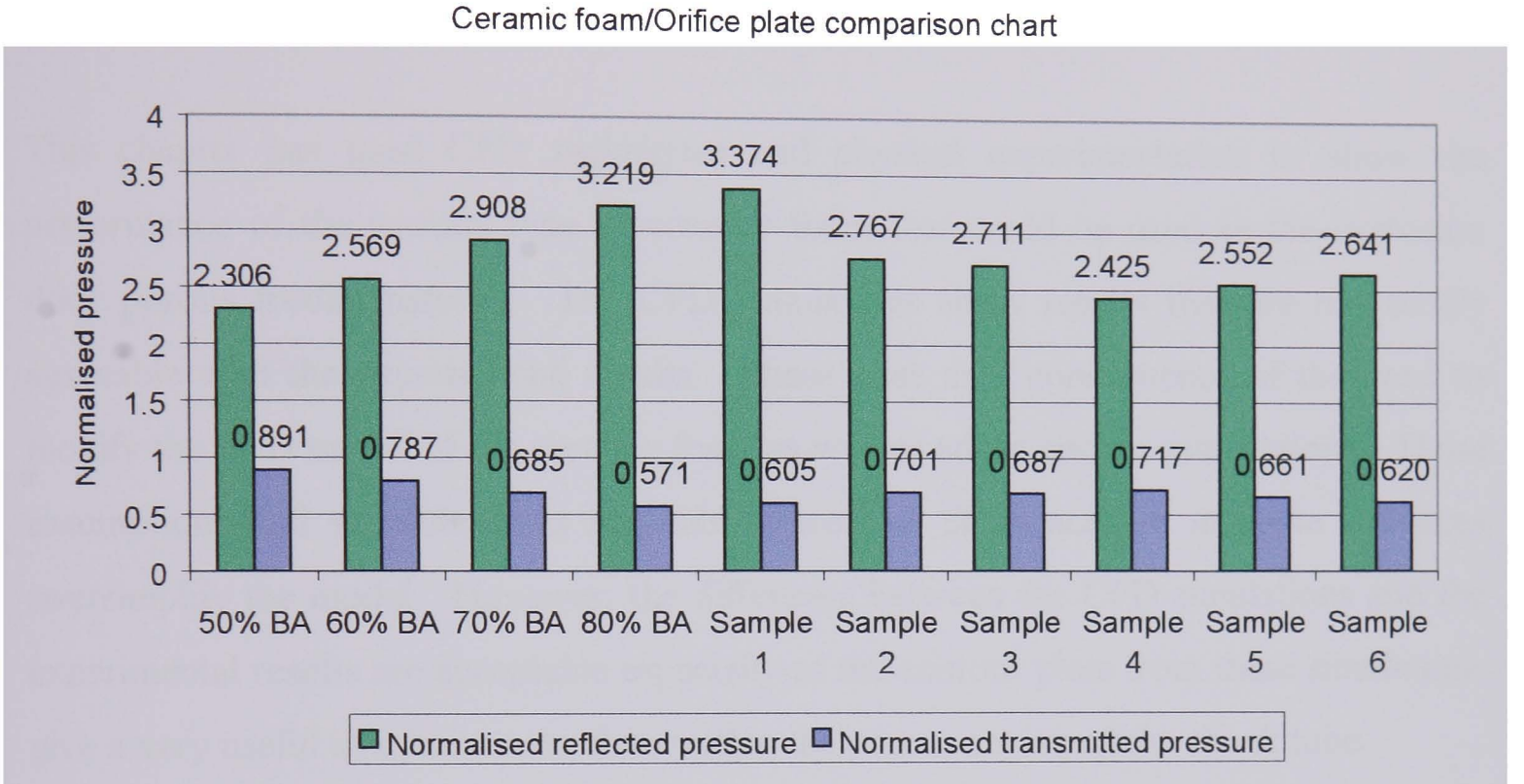

Figure 6.29 – Ceramic foam and orifice plate results – reflected and transmitted pressures.

The transmitted pressure is the property of interest – as it is the shock attenuation that will determine the usefulness of the ceramic foams to be used in the explosion door described earlier. The following observations were made from the experimental tests for the orifice plates and the ceramic foams.

- the pressure transmitted across the 70% BA orifice plate and the sample 3 ceramic foam are similar,
- the reflected pressure characteristics, though not particular important are presented for comparison purposes.

- the pressure reflected by the 60% BA orifice plate and the sample 5 ceramic foam are similar, and

- a 50% BA orifice plate and a sample 4 ceramic foam reflected the incident shock wave with similar magnitudes.

6.8 Conclusion

This chapter has used CFD techniques and physical experimentation to show the performance of the various type of ceramic foam that could be used as the explosion door porous media material. The CFD simulations show results that are not totally agreeable with the experimental results. These arise as a consequence of the need to modify the CFD model of the ceramic foam as well as adopt certain assumptions. These assumptions and simplifications invariably introduce differences or in some instances oversimplify the model. However, the difference between the CFD simulations and the experimental results are acceptable especially as the contour plots from these simulations give a very useful insight into the flow within the porous region of the shock tube.

The main points from this chapter are that:-

- there is a correlation between the pressure drop and the thickness of the ceramic foam for a given ppi value,

- the ceramic foams are strong enough to withstand high Mach number shock waves without sustaining any significant damage,

- the performance of the ceramics in terms of their pressure drop is similar, with a 14% change in transmitted pressure as the ppi value increases from 10 to 20 [these are samples 4, 5, and 6],

- the thin orifice plate performance characteristics are similar to the ceramic foam tests when the BA values are in the region of 60% and 70%,

- orifice plates with high BA values induce severe oscillations resulting in high reflected pressures, and subsequently low transmitted pressures, and
- the CFD model of the ceramic foam shows the behaviour of the flow around the obstructions in the shock tube, especially the high velocity region just downstream of the obstructions.

CHAPTER 7 Summary of main findings

7.1 Introduction

All experimental and computational simulation results were reported and discussed in chapter six. The performance of the porous media, the ceramic foam, and that of the orifice plates were shown through their pressure attenuation characteristics. This performance data was obtained by impinging upon the ceramic foam and thin orifice plate a shock wave with incident Mach numbers of 1.5. With the initial boundary condition of an 8.38:1 diaphragm pressure ratio, an incident pressure of 2.65 bar was obtained for the computational simulations and an average of 2.3 bar for the experimental tests. The difference in the incident pressure values for the same diaphragm pressure ratio was due to experimental losses. Further 'what if' simulations were conducted on the CFD model of the ceramic foam to determine the effects of increasing porosity on the smaller of the ceramic foam tested.

The intention of this chapter is to collate the data from the previous chapter and relate these results to the explosion door, especially the performance of the ceramic foam in minimising the pressure drop across it as a shock wave passes through. The following findings are meant to satisfy the objective of evaluating the performance of the ceramic foam as an explosion attenuation porous media. The ceramic foam will be part of an explosion door to be used in underground mining environments. Its primary function is to minimise the pressure drop across the explosion door as the shock wave passes through. By so doing, there is the likelihood of the explosion door (and the ceramic foam) remaining intact after the passage of the shock wave. This will increase the chances of the explosion door being able to arrest the flames that will be travelling behind the shock.

Thus, the contribution to knowledge is the performance characteristics of these ceramic foams along with the 'equivalency' chart for the thin orifice plates and the ceramic foams. The 'equivalency' chart is meant to define a property of the ceramic foam in terms of a blockage area. The pores per inch (ppi) value and their air porosity currently

describe the ceramic foams. The air porosity is based on the bulk density and the material density of the ceramic foam - showing a percentage air of the ceramic foam.

7.2 *The performance of the thin orifice plates – experimental tests and CFD simulations*

Tests were conducted on single and multiple hole orifice plates to determine the effect of the hole configuration on the performance of the orifice plates. However, as will be discussed later, all correlation data were obtained from the single hole orifice plates. The orifice plates tested were thin at 2 mm with a diameter of 55 mm. CFD simulations were also carried out for the orifice plates. These simulations were done in two dimensions and were intended to help with the validation of the experimental results as well as providing detailed graphic illustrations of the interaction of the shock wave with the thin orifice plates.

All the pressure values were normalised. The orifice plate experimental and CFD simulation results can be summarised as (see Figure 6.3, repeated here as Figure 7.1):-

- at all blockage areas, there is good agreement between the CFD simulations and the experimental test results for the transmitted pressure magnitudes. The margin between the highest and lowest transmitted pressure magnitudes is 6%,
- between 30% BA and 60% BA, the reflected pressure magnitudes from the CFD simulations and experimental results are within a margin of 8%,
- the margin between the reflected pressure magnitudes from the CFD simulations and the experimental results increases to 13% once the BA value is 70% and more,
- at low BA values (30%, 40%, and 50%), the rate of transmitted pressure drop is small. This shows that at low BA values the orifice plate does not adversely affect the transmitted pressure.
- as will be discussed in section 7.5, the performance of the ceramic foam is equivalent to orifice plates with BA values between 60% and 70%.

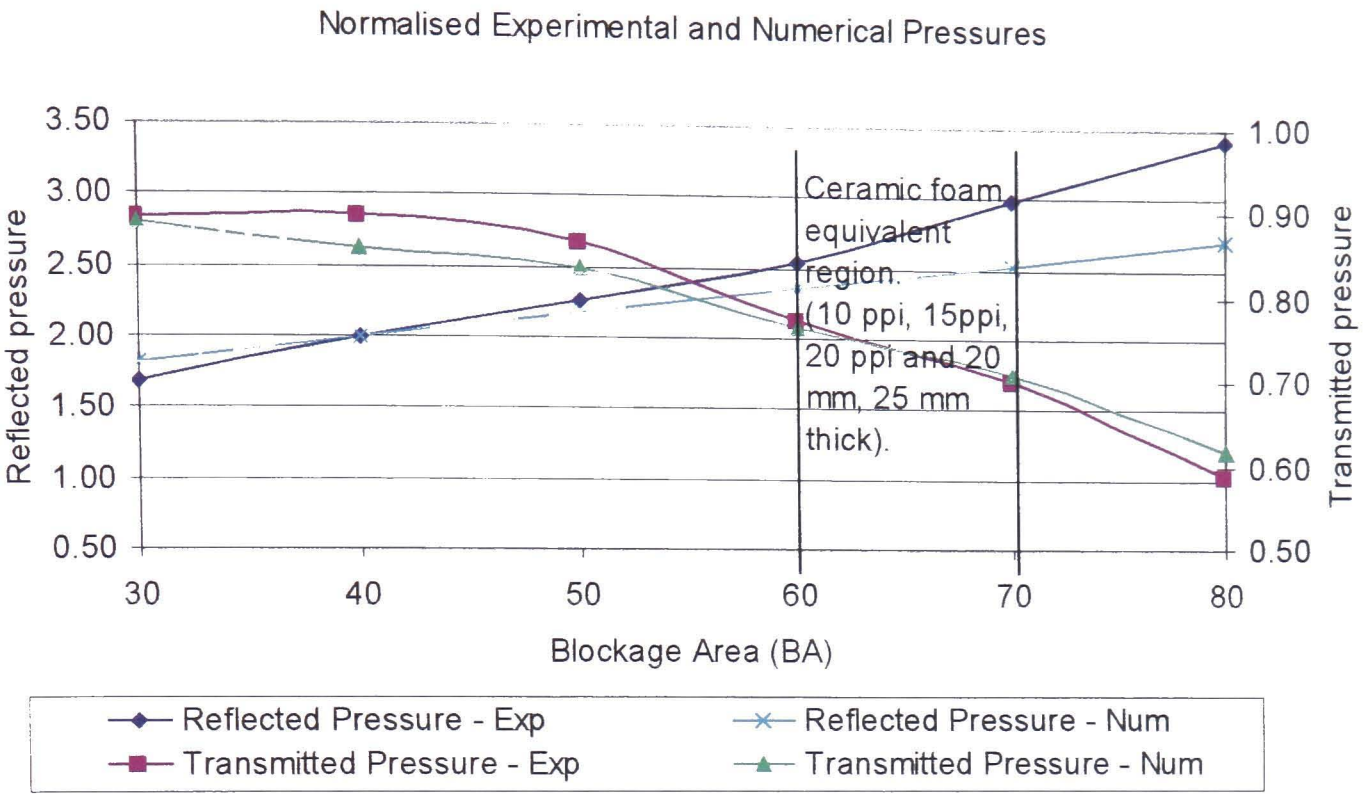

Figure 7.1 – Orifice plate results – experimental and CFD simulations.

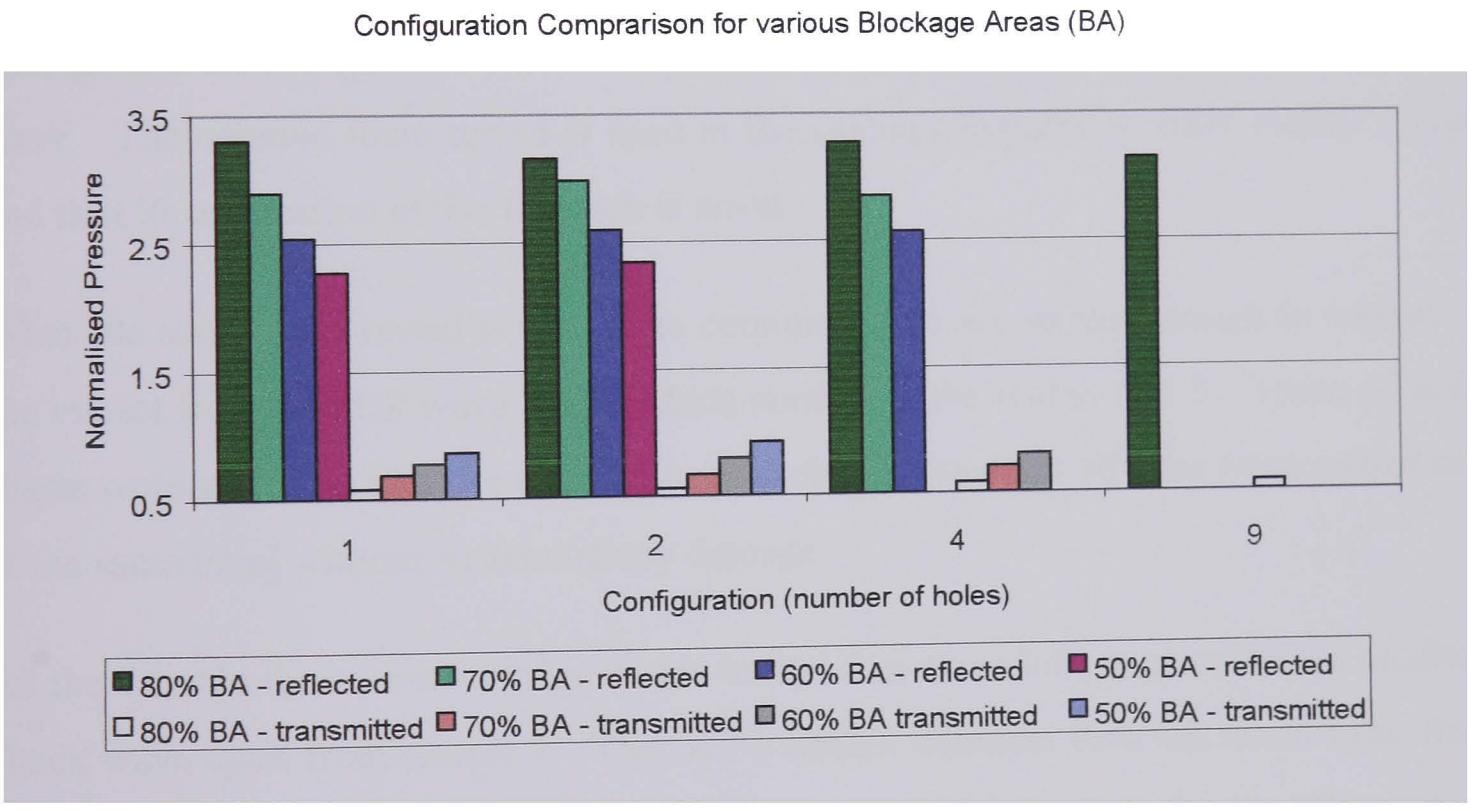

Figure 7.2 – Multiple hole configuration orifice plate results – experimental and CFD simulations

7.3 The performance of the thin orifice plates – multiple hole configuration

The effect of the hole diameter and the number of holes based on the same blockage area were investigated to determine their influence on the performance of the orifice plates. (See Figure 6.5 repeated here as Figure 7.2).

- the experimental results showed that the pressure drop across the orifice plate is independent of the number of holes and the hole configuration.

7.4 The performance of the ceramic foam – experimental and CFD simulations

The performance of the ceramic foam is the *raison d'être* of this research. In attenuating the shock wave preceding an explosion, the ceramic foam is meant to minimise the pressure drop across it. The pressure drop will be such that it will not sustain any damage and stand a good chance of arresting the flame front travelling behind the shock wave. The ceramic foam tested is used in the castings industry to filter molten metals and thus its application in this research is novel.

What the test results reveal is that these ceramic foams are strong enough to withstand the impact from a shock wave with a Mach number in the region of 1.5. These ceramic foams were subjected to more than ten tests each [note that not all tests were carried out at the same time] without sustaining any damage.

All the ceramic foams were similar in size in that they were fully exposed to the incident shock wave apart from sample 1. This had a smaller diameter than the shock tube, thus the pressure magnitudes are slightly different from the other ceramic foams. (See Figure 7.3). The results (experimental) are summarised based on the findings from the samples 2, 3, 4, 5, and 6.

- as the ppi value increases, the transmitted pressure decreases and the reflected pressure increases,

- it is suggested that the ceramic foams are strong enough to be used as the porous media in the explosion door,
- the ppi values affect the reflected pressure magnitude more than the transmitted pressure,
- the thickness of the ceramic foam affects the pressure transmitted for a given ppi value,
- the transmitted pressure magnitudes are within a margin of 14% for the 10 ppi sample 4 ceramic foam and the 20 ppi sample 6 ceramic foam, and
- based on the ceramic foam results, they can be classified as having the same pressure attenuation characteristics as thin orifice plates with BA values between 60% and 70%.

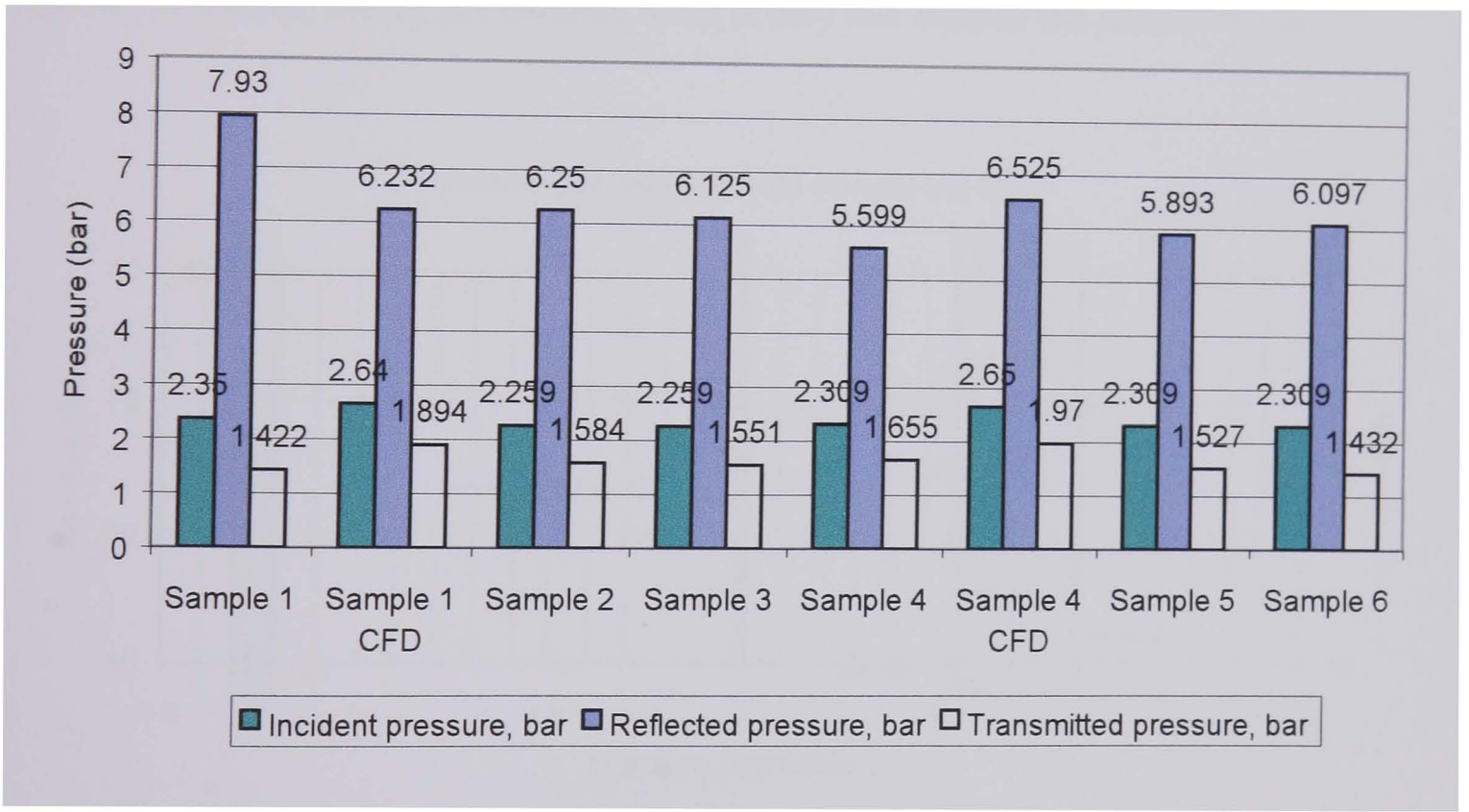

Figure 7.3 – Ceramic foam results – experimental and CFD simulations.

7.5 Comparison of the ceramic foam and orifice plates results – experimental and CFD simulations

One of the objectives of testing the orifice plates was to draw up an equivalency chart (see Figure 7.4) between the results obtained from such tests and that obtained from the ceramic foams. Such data would allow correlation between the orifice plates and the ceramic foams and give the ceramic foams a property based on the BA value of the orifice plates.

Figure 7.4 shows the equivalency chart for the ceramic foams and the orifice plates. The points on the chart are divided into the two pressure regions - reflected and transmitted.

For the reflected pressures, the shaded area represents the boundaries of the reflected pressure magnitudes for the 60% BA orifice plate and the 70% BA orifice plate. The two 20 ppi ceramic foams (samples 3 and 6) tested lie within the shaded region, one of the 15 ppi ceramic foams (sample 2) also lie within the shaded region. The 10 ppi ceramic foam (sample 4) and the 15 ppi ceramic foam (sample 5) are outside the shaded region. However, the 15 ppi ceramic foam is only just outside the shaded region.

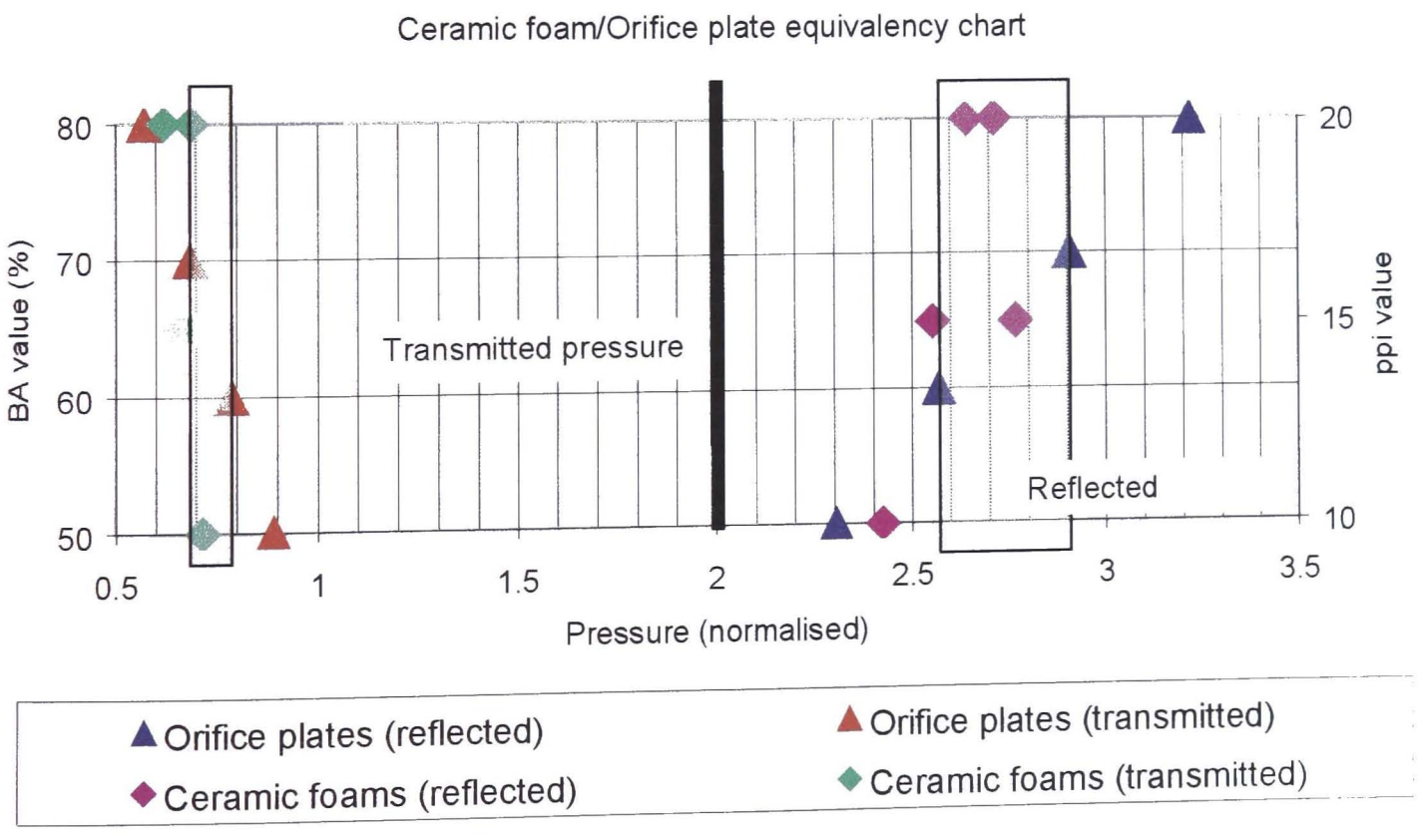

Figure 7.4 - Ceramic foam/Orifice plate equivalency chart.

The smaller shaded region in Figure 7.4 shows the transmitted pressure boundaries for the 60% BA orifice plate and the 70% BA orifice plate. Here, the 10 ppi ceramic foam (sample 4), one of the 15 ppi ceramic foams (sample 2), and the sample 3 ceramic foam (20 ppi) all lie within the 60% BA and 70% BA bounded region. The sample 5 ceramic foam (15 ppi) lies just outside the shaded region as does the 20 ppi (sample 6) ceramic foam.

These results show that the ceramic foams tested do have the characteristics of orifice plates with blockage areas within 60% and 70%.

The following points can be noted based on the experimental results of the ceramic foams and the orifice plates. (See Figure 6.29, repeated here as Figure 7.5).

- at high blockage areas, the orifice plates have a small area open to the incident shock wave. Thus, the reflected pressure magnitudes are much higher than that for orifice plates with lower blockage areas,
- the orifice plates are very thin (2 mm) compared to the ceramic foams (20 mm and 25 mm),
- by taking the transmitted pressures in isolation, the correlation between the results of the ceramic foams and the orifice plates show that they are similar in their transmitted pressure characteristics,
- likewise, if the reflected pressures are taken in isolation, then there is good agreement between most of the orifice plate and ceramic foam results,
- most of the ceramic foams tested have pressure attenuation characteristics that are equivalent to orifice plates with blockage areas between 60% and 70%. Thus the ceramic foams tested can be thought of as having the BA values between 60% and 70%.

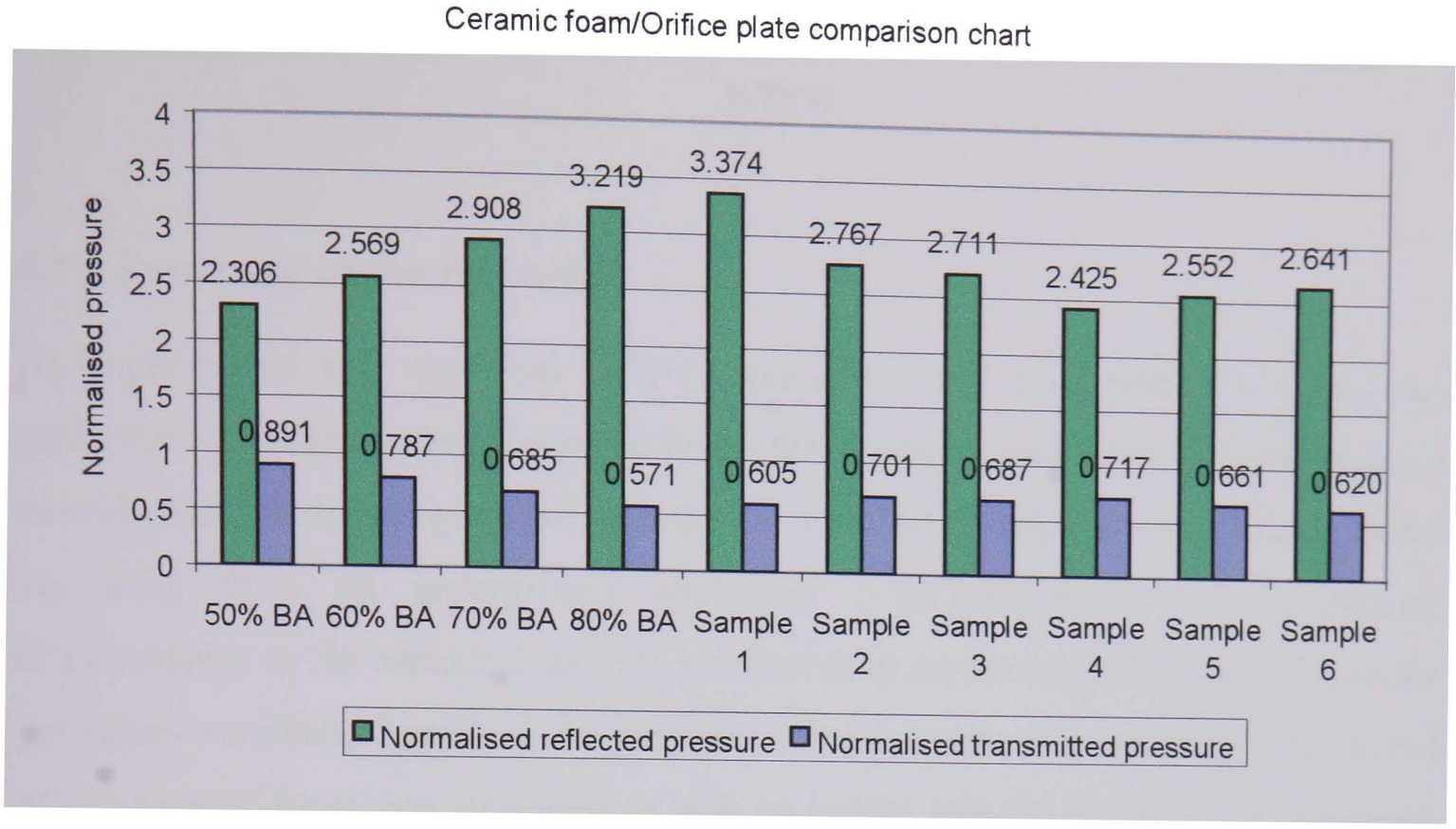

Figure 7.5 - Ceramic foam and orifice plate experimental results.

7.6 Conclusion

The main summary from the ceramic foam and orifice plate experimental tests and CFD simulations has been reported. In this chapter, the aim was to draw upon the results in chapter six and relate them to the explosion door. How the performance of the ceramic foam could be related to that of thin orifice plates was also discussed in this chapter.

Being able to describe the ceramic foam in terms of a blockage area characteristic of the thin orifice plates is particularly useful as there is no such designation for the ceramic foams. As reported earlier, their ppi value and their air porosity designate the ceramic foams. What this chapter has shown is that the ceramic foams tested have an equivalent blockage area of 60% to 70%.

The next chapter (eight) summarise the research work carried out and puts forward some ideas for future study.

CHAPTER 8 Conclusions and recommendations for further work

8.1 Summary of the research

An experimental and numerical (CFD) investigation has been carried out into the performance characteristics of ceramic foams that could be used as the porous media to minimise the pressure drop across an explosion door and subsequently arrest flame fronts emanating from an underground explosion. To determine the performance characteristics of the ceramic foam, the pressure drop across ceramic foam with various ppi values were investigated using a purpose built shock tube. An equivalent CFD model of the ceramic foam was simulated to give an insight into the behaviour of the shock wave around the vicinity of the ceramic foam, within the test section of the shock tube, and provide useful data for comparison purposes.

Thin orifice plates were also tested to provide data that could used in correlation with the results from the ceramic foam and an equivalency chart was produced. CFD simulations were also conducted on the thin orifice plates. All CFD simulations were done in two dimensions.

Chapter two gave an overview of coal and dust explosions, particularly the mechanisms which cause the initiation of methane explosions and subsequent coal dust explosions. Once these explosions are initiated, the current methods for arresting these underground explosions was discussed in **chapter three**. The current barriers, active and passive, together with the new explosion door were introduced.

In **chapter four**, an introduction to computational fluid dynamics provided the basis on which all the simulations conducted in this research were done. The tool used in the simulations was introduced. The role of CFD is to augment the experimental tests wherever possible and in other cases provide a useful insight into the flow domain, especially when no amount of experimentation can provide such detail. The intention of chapter four was to provide the reader with a basic understanding of CFD and how it

could be applied to the modelling of the shock tube and in particular, the ceramic foam and the orifice plates. However, certain assumptions have to be made when simulating the 'real' problem using CFD. Thus the assumptions adopted in using CFD to simulate the experimental tests were described in **chapter five** along with the experimental set-up and the porous media – the ceramic foam. A brief overview on shock tube flow was given as well as the specification of the experimental shock tube. This shock tube was built and subsequently modified at Brunel University. Initial validations tests were reported in chapter five. These tests consisted of simulating the flow in a two-dimensional model of the shock tube with no obstructions and conducting a simulation of the experimental problem. Also, as the shock tube flow can be solved analytically, results were obtained from all three tests and compared.

All CFD simulations and experimental results for the ceramic foam and the orifice plates were presented in **chapter six**. Here the aim was to present the raw results as taken from the various tests and determine the trends, characteristics, and suitability of the results for 'normal' use. Discussions on all the tests were done to show the performance characteristics of the ceramic foam and the possibility of correlating this performance with that from thin orifice plates. The CFD simulations in particular provided a useful insight into the behaviour of the shock wave around the region of the orifice plate or the CFD model of the ceramic foam, and in some instances revealed potential problems that the experimental tests could not reveal. In **chapter seven**, special attention was paid to the usefulness of the data from the various tests conducted to the explosion door. The ability of the ceramic foam to minimise the pressure drop across itself as the shock wave passes through the explosion door and arrest flame fronts were discussed. Here, the data that would be particularly useful in the design of the explosion door was presented, namely the performance of the various ceramic foams with their respective ppi values. The pressure drop across these ceramic foams, the reflected pressure, and in particular, the transmitted pressure were also reported.

8.2 Main Conclusions

The overriding aim of this research was to investigate the performance of ceramic foams in their application as the porous media in an explosion door. By minimising the magnitude of the pressure drop across itself as a shock wave passes through the explosion door, the ceramic foam would stand a good chance of not being destroyed. If the ceramic foam (and the explosion door) are not destroyed, then further research can investigate the likelihood of the flame front behind the shock wave being arrested.

This intended application of the ceramic foam is novel to the world of underground mining and its successful application will improve the level of safety already prevalent in the industry. Thus, the main conclusion that can be drawn from this research is that ceramic foams have the ability to reduce the strength of strong shock waves travelling at Mach 1.5. The magnitude of the pressure drop is dependent on the ppi value of the ceramic foam as well as its thickness.

The following points can be drawn from the experiments and simulations carried out as part of this project:-

1) This importance of being able to minimise the pressure drop across the ceramic foam without sustaining any damage is critical to the use of ceramic foams.

2) It was found that the ceramic foam could fail after several tests. With safety being critical, these ceramic foams should certainly be changed after an incident.

3) The differences between the ceramic foams in terms of their ppi values does reflect on their performance though not to a great extent. Simply put, the pressure drop across a ceramic foam having a 10 ppi structure is only 14% less than the pressure drop across a 20 ppi ceramic foam.

4) The ceramic foams tested can be thought of as having blockage areas between 60% and 70%. This is a useful characteristic as the ceramic foams in general do not have such a designation.

5) CFD simulations greatly enhance the experimental tests and if certain assumptions are made, they can produce results that are close to that from the experiments. The porous media model in Rampant was unable to correctly predict the transient flow through the ceramic foam.

6) Shock tubes are a useful aid to simulating the effects of explosion pressures without incurring the high costs of creating explosions outside of the laboratory.

7) The ceramic foams have been shown to be capable of minimising the pressure drop across itself without sustaining any damage. It is therefore possible that they could in a state to arrest the flame front travelling behind the shock.

These conclusions point the way forward to the possibility of making underground mines a safer environment through the provision of data on the ceramic foam that would form part of the explosion door discussed earlier.

This contributes to the body of knowledge in the field of safety not just in underground mines but to any industry that suffers from the risk of explosions.

The need to the minimise pressure drop across the ceramic foam and arrest the flames would thus realise the full potential of the ceramic foam not just as a filter material but as a multi-purpose material that could potentially save lives.

8.3 Recommendations for further research

The work reported in this research was carried out within constraints laid down by the materials being used:-

- the shock tube material could not operate safely in pressures greater than 10 bar,
- the CFD porous media model could not accurately model the transient flow in any porous media, and
- the ceramic foams were between 20 mm and 25 mm thick.

Whilst these are not faults, in fact, this being the first series of tests done on ceramic foams to produce such performance data, the equipment, materials, and all other tools can only be improved upon.

1) Thus, further research at high Mach numbers and incident pressures could further investigate the ability of the ceramic foams to successfully perform in underground mining environments without failure.

2) Increasing the thickness of the ceramic foams or better still, using two ceramic foams in tandem could provide more data on shock wave attenuation.

3) A more robust representation of porous media in the software code, Rampant, would greatly improve the ability to draw more detailed comparisons from the CFD simulations and the experimental tests. In short, a more realistic model of porous media is needed.

4) All CFD simulations were done in two dimensions. Further simulations in three dimensions, though time consuming could validate the two-dimensional simulations.

5) More tests on ceramic foams with different ppi values to further determine their performance and correlate these to that from thin orifice plates.

6) Investigate the ability of the ceramic foams to arrest flames with the knowledge that they can withstand the impact from shock waves without sustaining any damage.

7) Investigate the feasibility of incorporating the ceramic foam into long thin pipes carrying flammable/explosive materials as in the oil industry.

References

[1] Cybulska, R. Examples of coal dust explosions. *Proceedings of the Australian. IMM Illawarra Branch: Ignitions, Explosions and Fires in Coal Mines Symposium*, May 1981, p.7.1-7.13.

[2] Michelis, J. and Kleine, W. Development of components, designed to resist explosion pressures of approximately 1 MPa, for use in ventilation structures in underground mines. *Unpublished work.*

[3] Rogg, B., Hermann, D., and Adomeit, G. Shock-induced flow in a porous medium. *Proceedings of Euromech 143, Delft*, September 1981, p.3-9.

[4] Levy, A., Ben-Dor, G,. Skews, B.W., and Sorek, S. Head-on collision of normal shock waves with rigid porous materials. *Experiments in Fluids 15*, 1993, p.183-190.

[5] Mines and Quarries Acts (1954), The law relating to safety and health in mines and quarries. *Part 1 – The Act, Part 2 – The Regulations.* HMSO, 1954.

[6] Essenhigh, R.H. Dust explosion research. *Journal of Loss Prevention 2*, 1968, p.44-53.

[7] Hertzberg, M., and Cashdollar, K.L. Introduction to dust explosions, Industrial dust explosions. ASTM STP 958, K.L. Cashdollar and M. Hertzberg (Eds.), *American Society for Testing Materials, Philadelphia*, 1987, p.243-264.

[8] Ogle, R.A., Beddow, J.K., and Vetter, AF. Numerical modelling of dust explosions: The influence of particle shape on explosion intensity. *Proceedings of the Technical Programme: International Powder & Bulk Solids Handling and Processing*, 1983, p.176-195.

[9] Garcia Torrent, J., and Cantalapiedra Fuchs, J. On the combustion mechanism of coal dust. *Combustion and Flame*, December 1991, Vol. 87, Nos. ¾, p.371-374.

[10] Dust Explosions. *Building Research Establishment Digest*, Digest 288, August 1984. pp.6.

[11] Kinney, G.F., and Graham, K.J. *Explosive shocks in air*. Springer-Verlag, 1985.

[12] Powell, F., Billinge, K., and Cutler, D.P. The ignition of methane-air by machine picks cutting into rock. *16th International Conference of Safety in Mines Research*, Washington DC, 1975.

[13] Griffith, W.C. Dust Explosions. *Annual Review Fluid Mechanics*, Vol. 10, 1978, p.93-105.

[14] Rae, D. Initiation of weak coal dust explosions in long galleries and the importance of the time dependence of the explosion pressure. *14th International Symposium on Combustion*, The Combustion Institute, Pittsburgh, 1988, p.1225-1234.

[15] Gardner, B.R., Winter, R.J., and Moore, M.J. Explosion development and deflagration-to-detonation transition in coal dust/air suspensions. *14th International Symposium on Combustion*, The Combustion Institute, Pittsburgh, 1988, p.335-343.

[16] Phylaktou, H., and Andrews, G.E. Gas explosions in long closed vessels. *Combustion Science and Technology*, Vol. 77, 1991, p.27-39.

[17] Phillips, H. Aerodynamic roughness and flame propagation in models of methane explosions. *12th International Conference of Mine-Safety Research Establishments*, Dortmund, 1967.

[18] Edwards, J.C., and Ford, K.M. Model of coal dust explosion suppression by rock dust entrainment. Report of Investigations – *United States Bureau of Mines*, 1988, No. 9206.

[19] Artingsall, G., and Corlett, T.C. The effect of reflected pressure waves on the propagation of dust explosions. *Restricted International Conference of Directors of Safety in Mines Research*, Sheffield, 1965.

[20] Vos, A.D. Coal dust explosions, their prevention and control. *Journal of Mine Ventilation of South Africa*, 1974, June, Vol. 27, p.81-86.

[21] Cybulski, W. Coal dust explosions and their suppression. *Warsaw: Foreign Scientific Publications Department of the National Centre for Scientific and Economic Information*, 1975.

[22] Umezu, M., Matsukuma, K., Yotsumoto, Y., and Higuchi, K. Combustion and explosion of methane layer in roadways forming branch structure . *Unpublished work.*

[23] Cybulska, R. Examples of coal dust explosions. *Proceedings of the Australian IMM Illawarra Branch, Ignitions, Explosions of Fires in Coal Mines Symposium*, p.7.1-7.13, 1981.

[24] Lee, J.H.S. Dust explosions: An Overview. *Shock Tubes and Waves, Proceedings of the 16th International Symposium on Shock Tubes and Waves*, Achen, West Germany, July 26-31, 1987.

[25] Bardon, M.F., and Fletcher, D.E. Dust Explosions. *Scientific Progress*, Oxford, Vol. 68, No. 272, 1983, p.459-473.

[26] Zeeuwen, J.P. A practical look at explosion characteristics. *Proceedings of the First International Symposium on Explosion Protection in Practice, Part 2: Dust explosion protection*, 1984, pp.17.

[27] Powell, F., and Billinge K. The use of water in the prevention of ignitions caused by machine picks. *Mining Engineer*, August 1981, Vol. 141, No. 239, p.81-85.

[28] Cashdollar, K.L. Coal dust explosibility. *Journal of Loss Prevention in the Process Industries*, 1996, Vol. 9, Part 1, p.65-76.

[29] Franke, H. Determination of minimum ignition energies of coal dust-methane-air mixtures (Hybrid mixtures). *17th International Conference of Directors of Safety in Mines Research*, Varna, October 1977, p.1-5.

[30] Skews, B.W., and Law, W.R. The propagation of shock waves in a complex tunnel system. *Journal of the South African Institute of Mining and Metallurgy*, Vol. 91. Part 4, 1991, p.137-144.

[31] Amyotte, P.R., Chippett, S., and Pegg, M.J. Effects of turbulence on dust explosions. *Progress in Energy and Combustion Science*, Vol. 14, Part 4, 1989, p.293-310.

[32] Lunn, G.A., and Roberts, A.F. Recent trials with coal dust/methane hybrid explosions. *22nd International Conference*, SMRI, Beijing, 1987.

[33] Moen, I.O., Donato, M., Knystautas, R., and Lee, J.H. Flame acceleration due to turbulence produced by obstacles. *Combustion and Fame*, Vol. 39, 1980, p.21-32.

[34] Hjertager, B.H. Explosions in obstructed vessels. *Explosion Prediction and Mitigation Conference*, Leeds, 1995.

[35] Lunn, G.A. Vent design for near cubical vessels and estimation of reduced pressures. *Explosion Prediction and Mitigation Conference*, Leeds, 1995.

[36] Alexiou, A., Phylaktou, H., and Andrews, G.E. Vented gas explosions in a long vessel with obstacles. *Institution of Chemical Engineers Symposium Series*, 1995, No. 139, p.297-312.

[37] Lebecki, K. Research on the theory of dust explosions. *12th International Conference of Mine-Safety Research Establishments*. Dortmund, 1967, pp.20.

[38] Popat, N.R., Catlin, C.A., Arntzen, B.J., Lindstedt, R.P., Hjertager, B.H., Solberg, T., Saeter, O., and Van den Berg, A.C. Investigations to improve and assess the accuracy of computational fluid dynamics based explosion models. *Journal of Hazardous Materials*, Vol. 45, Part 1, 1996, p.1-25.

[39] Lea, C.J. Computational modelling of mine fires. *Proceedings of the 25th International Conference of Safety in Mines Research Institutes*, Johannesburg, South Africa, 1993 p.19-34.

[40] Caulfield, C.P., and Linden, P.F. Smoke movement in tunnels: The interface of the near-fire model with MFIRE. Report NO. FM 53/91, *Cambridge Environmental Research Consultants, prepared for the UK Health and Safety Executive*, 1991.

[41] Pantaker, S.V. *Numerical heat transfer and fluid flow*. Hemisphere Publishing Corporation, 1980.

[42] Suzuki, T., and Adachi, T. A blast wave propagating over the dust deposited on a floor. *Proceedings of the 14th International Symposium on Shock Tubes and Waves*, Sydney, August 1983, p.489-496.

[43] Skews, B.A., and Law, W.R. The propagation of shock waves in a complex tunnel system. *Journal of the South African Institute of Mining and Metallurgy*, Vol. 91, Part 4, 1991, p.137-144.

[44] van den Berg, A. C., van Wingerden, C.J.M., and The, H.G. Vapour cloud explosion blast modelling. *IChemE Symposium No. 124*, 1991, p.393-409.

[45] Bartknecht, W. *Explosions: course, prevention, protection*. Springer-Verlag, Berlin. 1981.

[46] Field, P. *Dust explosions, Volume 4 – Handbook of powder technology*. Elsevier, Amsterdam. 1982.

[47] Nagy, J., and Verakis, H. Development and control of dust explosions. *Marcel Dekker*, New York. 1983.

[48] Cybulski, W. Coal dust explosions and their suppression. (translated from Polish), TT 73-54001, *National Technical Information Service, US Department of Commerce*, Springfield, VA. 1975.

[49] Cybulski, W. General formulae embracing the protection of coal dust against the propagation of explosion. *International Conference of Safety in Mines Research*, Tokyo, 1969, pp.19.

[50] Cybulska, R., and Cybulski, K. Combating methane explosions by means of water barriers. *19th International Conference of Research Institutes in Safety in Mines*, Katowice, Poland, October 1981.

[51] Cybulski, W. Research on the effectiveness of stone dust barriers for stopping the coal dust explosions, depending on their arrangement in the cross-section of the gallery. *12th International Conference of Mine-Safety Research Establishments*, Dortmund, 1967.

[52] Cybulski, W. Effectiveness of stone-dust barriers for stopping the explosions of coal dust at greater distances from the spot of initiating the explosion, and comparison of the effectiveness of stone-dust and water barriers. *Restricted International Conference of Directors of Safety in Mines Research*, Sheffield, July 1965.

[53] Meerbach, H., and Michelis, J. Examination of the protection against pit explosions which take place one after the other in the same roadway. *18th International Conference of Mining Safety Research*, Yugoslavia, 1979, pp.10.

[54] Edwards, J.C., and Ford, K.M. Model of coal dust explosion suppression by rock dust entrainment. *Report of Investigations – United States Bureau of Mines*, 1988, No. 9206.

[55] Liebman, I., and Richmond, J.K. Ranking of extinguishing agents against coal dust explosions. *International Conference on Scientific Research in the field of Safety at Work in the Mining Industry*, October 1979. Paper B6.

[56] Hinsley, R.S. The design of triggered barriers for arresting mine explosions. *14th International Conference of Mine-Safety Research Establishments*, Section 2 – Suppression of Firedamp and Coal-Dust Explosions, 1971.

[57] Sapko, M.J., Greninger, N.B., and Watson, R.W. Review paper: Prevention and suppression of coal mine explosions. *Proceedings of the 23rd International Conference of Safety in Mines Research Institutes*, Washington, DC, Sept. 11-15, 1989.

[58] Liebman, I., Richmond, J.K., and Grumer, J. Recent developments in passive and triggered explosion barriers. *16th International Conference on Coal Mine Safety Research*, Washington DC, September 1975, p.VII 4.1-VII 4.18.

[59] Kawenski, E.M., Nagy, J., and Conn, J.W. Further development of an explosion quenching device. *International Conference of Safety in Mines Research Establishments*, Dortmund, 1969.

[60] Fisher, T.J., and Cohen, A.F. Sensor location strategy for minewide environmental monitoring. *Proceedings of the 21st International Conference, Safety in Mines Research Institutes*, Sydney, Australia, October 1985, p.393-398.

[61] Jones, T.A., and Bott, B. A multisensor system for mine atmosphere monitoring. Proceedings of the *21st International Conference in Mines Research Institutes*, Sydney, Australia, October 1985, p.399-404.

[62] Faber, M., and Scholl, E-M. Automatic suppression of multiple explosions in underground coal mines. *21st International Conference of Safety in Mines Research*, Sydney, 1985, p.645-649.

[63] Cortese, R.A., and Sapko, M.J. Flame powered trigger device for activating explosion suppression barrier. *Proceedings of the US Mine Ventilation Symposium*, Vol. 199, 1991, p.458-466.

[64] Cybulski, W. Studies of triggered barriers. *15th International Conference on the Safety in Mines Research*, Karlovy Vary, Czechoslovakia, September 1973, p133-146.

[65] Cybulski, W. The recent testing results of the Barbara Experimental Mine in the field of coal dust and methane explosions. *International Conference of Safety in Mines Research*, Tokyo, 1969, pp.30.

[66] Meerbach H., and Michelis, J. The Tremonia triggered barrier. *Glueckauf* with English translation, Vol. 116, No. 16, p.347-351.

[67] Cybulski, W. Effectiveness of stone-dust barriers for stopping the explosions of coal dust at greater distances from the spot of initiating the explosion, and comparison of the effectiveness of stone-dust and water barriers. *Restricted International Conference of Directors of Safety in Mine Research*, Sheffield, 1965.

[68] Winter, J., and Giltaire, M. Experiments with rock dust or water barriers and a triggered barrier for the protection of dead-end workings. *15th International Conference of Mine Safety Research Establishments*, Karlovy-Vary, 1973.

[69] Meerbach, H. Investigation of the efficacy of water barriers in special conditions of application. *Proceedings of the 21st International Conference, Safety in Mines Research Institutes*, Sydney, Australia, October 1985.

[70] Dixon, D.W., Ediz, I.G., and Fidler, W.M. A new method for the arresting of underground tunnel explosions. *Proceedings of the 7th US Mine Ventilation Symposium, Lexington, Kentucky*, June 1995.

[71] Frolov, S.M., Gelfand, B.E., Medvedev, S.P., and Tsyganov, S.A, Quenching of Shock Waves by Barriers and Screens. *17th International Symposium on Shock Waves and Shock Tubes*, Bethlehem, PA, 1989, p.314-320.

[72] Phillips, H., and Pritchard, D.K. Performance requirements of flame arresters in practical applications. *Institute of Chemical Engineers Symposium Series*, Part 97, 1986, p.47-61.

[73] Dixon, D.W., Fidler, W.M., and Ediz, I.G. The preliminary analysis of the pressure wave transmission/reflection characteristics of explosion doors using one-dimensional finite isentropic wave theory. *Proceedings of the 9th Coal Congress of Turkey*, 1993, p.319-330.

[74] Wendt, J.F (ed.). *Computational Fluid Dynamics - An introduction*. Springer-Verlag, 1992.

[75] User's Guide for Fluent/Uns & Rampant, Release 4.0, Vol. 3 - Chapter 13 - *Physical Models for Flow and Heat Transfer in Rampant*, Fluent Inc., March 1996.

[76] Reynolds, O. *Phil Trans. of the Royal Society*, London, Series A, Vol. 186, 1874, p.123-161.

[77] Younis, B.A. Models of turbulence. Course notes - Introductory School in CFD (EPSRC CFD Community Club), *City University*, 1995.

[78] Versteeg, H.K., and Malalasekera, W. *An introduction to Computational Fluid Dynamics* - The Finite Volume Method. Longman Scientific & Technical, 1995.

[79] Glass, I.I. *Shock Waves & Man*. University of Toronto Press, 1974.

[80] Anderson, J.D. *Modern Compressible Flow* - with Historical Perspective. 2nd Edition, 1990, McGraw-Hill.

[81] Glass, I.I., and Sislian, J.P. *Nonstationary Flows and Shock Waves*. Oxford Science Publications, Oxford University Press, 1994.

[82] Hirsch, C. *Numerical computation of internal and external flows, Volume 2 – Computational Methods for Inviscid and Viscous Flows*, John Wiley and Sons, 1988.

[83] Courant, R., and Fredrichs, K.O. *Supersonic flows and shock waves*. Interscience, New York, 1948.

[84] Toro, E.F., and Roe, P.L. A hybrid scheme for the Euler equations using the Random Choice and Roe's methods. Numerical Methods for Fluid Dynamics III, *Clarendon Press*, 1988, p.391-402.

[85] Sod, G.A. A survey of several finite difference methods for systems of non-linear hyperbolic conservation laws. *Journal of Computational Physics*, 1978, Vol. 27, p.1-31.

[86] Roberts, T.W. The behaviour of flux difference splitting schemes near slowly moving shock waves. Numerical Methods for Fluid Dynamics III, *Clarendon Press*, 1988, p.442-448.

[87] Meadows K.R., and Casper J. Computing unsteady shock waves for aeroacoustic applications. *AIAA Journal*, Vol. 32, No. 7, July 1994, p.1360-1366.

[88] Von Neumann, J., and Richtmeyer, R.D. *Journal of Applied Physics 21* (1950), 232.

[89] Cahen, J., Couaillier, V., Delery, J., and Pot, T. Validation of code using turbulence model applied to three-dimensional transonic channel. *AIAA Journal*, Vol. 33, No. 4, April 1995, p.671-679.

[90] Bonnet-Heude, N. Estimation of flow through porous and perforated plates with CFX and scale model validations. *Third CFX International Users Conference*, October/November 1996, p.589-600.

[91] Levy, A., Ben-Dor, G., Skews, BW., and Sorek, S. Head-on collision of normal shock waves with rigid porous materials. *Experiments in Fluids*, 1993 Vol. 15, p.183-190.

[92] Sutton, W.H., Palmer, J.C., and Morris, J.R., Development of ceramic foam materials for filtering high temperature alloys. *31st Annual Meeting, ICI*, Dallas, TX, 1983.

PUBLICATIONS

Dixon, D.W., Dwomoh, M., and Ediz, I.G. Current and Future Methods for the Prediction of Underground Methane Emission. *Proceedings of the 1st International Mine Environmental Engineering Symposium*, Kütahya, Turkey, July 1996.

Dwomoh, M., Dixon, D.W., and Ediz, I.G. The passage of shock waves through a permeable explosion door – A computational study. *15th Mining Congress of Turkey*, 1997, p.211-217.

Dwomoh, M., Wang, CJ., Dixon-Hardy, D.W., and Ediz, I.G. An investigation into the effects of an explosion in a tunnel. *2nd International Symposium on Mine Environmental Engineering*, 1998, p.224-230.

Dwomoh, M., Dixon-Hardy, D. Arresting underground tunnel explosions – A computational fluid dynamics study. *Mining Technology*. Under review.

Dwomoh, M., and Dixon-Hardy, D. Modelling obstructions in a shock tube: - The differences between an inviscid model and a turbulent model. *International Journal for Numerical Methods in Fluids*. Under review.